RSC Advances

PAPER

View Article Online
View Journal | View Issue

Cite this: *RSC Adv.*, 2019, **9**, 30462

Exploring half-metallic Co-based full Heusler alloys using a DFT+*U* method combined with linear response approach

Kenji Nawa *[a] and Yoshio Miura[abc]

A density functional theory (DFT)+*U* method based on linear response (LR) theory was applied to investigate the electronic structures of a Co-based ternary full Heusler alloy Co_2YSi to explore half-metallic (HM) ferromagnets with a wide HM gap. The LR-based DFT+*U* calculations tend to obtain a reasonable correlation parameter for the Y site, while the correlation of the Co site misdirects to the unphysical ground state due to the overestimated parameter value that arises from the delocalized electronic structure of Co. Furthermore, we found that the HM gap of Co_2MnSi originates from the Co e_u^* orbital in the conduction state and the Co–Mn hybridizing t_{2g} orbital in the valence state around the Fermi energy. This means that the HM gap is a tunable property by selecting the Y element and/or mixing several elements into the Y site through t_{2g} atomic-orbital coupling. Our LR-based DFT+*U* method was extended to other ternary Co_2YSi and quaternary $Co_2(Y,Mn)Si$. We found that $Co_2(Ti_{0.25},Mn_{0.75})Si$ and $Co_2(Fe_{0.25},Mn_{0.75})Si$ show HM nature, with the Fermi energy being at almost the center of the minority band gap, which leads to high thermal stability.

Received 9th July 2019
Accepted 29th August 2019

DOI: 10.1039/c9ra05212g

rsc.li/rsc-advances

1 Introduction

A key property in the emerging field of spintronics is the so-called half-metallicity (HM); the majority and minority states are completely spin-polarized at the Fermi level, where a finite density of states (DOS) exists for majority spin and an energy band gap is opened for minority spin. The use of HM materials as ferromagnetic electrodes in magnetic tunnel junctions (MTJs) is a straightforward way to enhance the tunneling magnetoresistance (TMR) ratio,[1] leading to high-performance spintronics applications such as non-volatile magnetic random access memories and the read-head of ultrahigh-density hard-disk drives. So far, many candidates have been proposed as HM materials, *e.g.*, zinc-blende structural materials,[2–4] colossal magnetoresistance materials,[5,6] oxides such as rutile CrO_2 (ref. 7–10) and spinel-type magnetite Fe_3O_4,[11,12] and diluted magnetic semiconductors (SnO_2, Y_2O_3).[13–15] Among them, the family of Co-based full Heusler alloys has received considerable attention, as some of these have the potential to possess a high spin polarization (P) or ultimately HM (P = 100%) in addition to a high Curie temperature, *e.g.*, 985 K for Co_2MnSi[16] and 1100 K for Co_2FeSi.[17,18]

The spin polarization of electrodes in an MTJ device can be evaluated using the Julliè model[1] with a simple formula $\mathrm{TMR} = \frac{2P_1P_2}{1-P_1P_2} \times 100(\%)$, where P_1 and P_2 are the tunneling spin polarizations of the two ferromagnetic electrodes in the MTJ. For a Co_2MnSi MTJ with an aluminum oxide (Al–O) barrier, Sakuraba *et al.* observed the spin polarization to be over 80%.[19,20] Then, a high value of 95.4%, which may be close to a fully spin-polarized electronic structure, was reported for the MgO barrier MTJ.[21] However, $P_{1(2)}$ in the Julliè formula is not the spin polarization in the bulk system but the polarization of the tunneling electrons in the MTJ. The electronic structure of the MTJ electrode differs from that of the bulk material because the band structure is drastically changed due to the interfacial effect arising from the insulating barrier. The tunneling electrons are also influenced by the spin-filtering effect.[22] These facts imply that there is difficulty in an accurate estimation of purely bulk spin polarization from the TMR of MTJ.

The point contact Andreev reflection (PCAR) technique has also been performed for spin polarization in several Heusler alloys. The conductance of metallic electrons is measured at a cryogenic temperature to evaluate the spin polarization in PCAR; hence, P_{PCAR}, referred to as PCAR-measured spin polarization, is expressed as $P_{\mathrm{PCAR}} = \frac{\langle N^{\uparrow}(E_F)v_F^{\uparrow}\rangle - \langle N^{\downarrow}(E_F)v_F^{\downarrow}\rangle}{\langle N^{\uparrow}(E_F)v_F^{\uparrow}\rangle + \langle N^{\downarrow}(E_F)v_F^{\downarrow}\rangle} \times 100(\%)$. Here, $N^{\sigma}(E_F)$ and

[a]*Research Center for Magnetic and Spintronic Materials (CMSM), National Institute for Materials Science (NIMS), 1-2-1 Sengen, Tsukuba, Ibaraki 305-0047, Japan. E-mail: nawa.kenji@nims.go.jp*

[b]*Center for Materials Research by Information Integration, National Institute for Materials Science (NIMS), 1-2-1 Sengen, Tsukuba, Ibaraki 305-0047, Japan*

[c]*Center for Spintronics Research Network (CSRN), Graduate School of Engineering Science, Osaka University, 1-3 Machikaneyama, Toyonaka, Osaka 560-8531, Japan*

v_F^σ are the DOS at the Fermi energy and the Fermi velocity with spin index $\sigma(=\uparrow$ or $\downarrow)$ in a diffusive regime[23,24] where the current electrons are not assumed to be ballistic because of the mean-free path being shorter than the point contact size in actual experiments. The v_F^σ is the conductance of the electrons, but the d orbital localized around the Fermi energy is not dominant in the current electrons. This indicates that the spin polarization originating from the d electron is lost in the measured P_{PCAR}. Previous work reported that the current spin polarization deduced by PCAR is only 59% for Co_2MnSi[25] and around 50% for Co_2FeSi.[26–28] $P_{PCAR} = 64\%$ is also observed in quaternary $Co_2(Fe,Mn)Si$.[29]

Another critical subject to overcome is the large temperature dependence of P.[19–21,26,30–33] Experimental studies have reported that although an extremely high value of TMR ratio is demonstrated at low temperature in the MTJs consisting of Heusler electrodes and an MgO barrier, a significant reduction in TMR at room temperature is observed: for example, in the Co_2MnSi/MgO/Co_2MnSi MTJ[21] the TMR at 4.2 K is 2010%, but it decreases to only 335% at 290 K and in $Co_2(Fe,Mn)Si$/MgO/$Co_2(Fe,Mn)Si$[34] the TMR at 4.2 K is 2610%, but only 429% at 290 K. From the Jullièr model, the spin polarization $P = 95\%$ (98%) at low temperature and decreases to $P = 79\%$ (82%) at room temperature for MTJs with a Co_2MnSi ($Co_2(Fe,Mn)Si$) electrode. A similar situation occurred in a current-perpendicular-to-plane giant MR (CPP-GMR) device composed of $Co_2(Fe,Mn)Si$ electrodes and a nonmagnetic Ag spacer.[30,32] To explain the strong thermal-dependence of TMR and GMR performances, it is known that the spin-flip inelastic tunneling process induced by magnon excitation lowers P in addition to spin-conserving elastic tunneling at increased temperatures.[21,31] In this sense, the width of the energy band gap in the minority state is also important in the search for HM materials to improve the weak resistivity with respect to temperature.

Ab initio calculations based on density functional theory (DFT)[35–37] are expected to play a leading role in the understanding of fundamental electronic and magnetic structures in material design using HM Heusler alloys. In the framework of DFT calculation within local spin density approximation (LSDA), Galanakis *et al.*[38] presented an energy diagram of the atomic orbital hybridization of the Co_2MnGe system to clarify the mechanism of the HM property; the minority energy band gap at the Fermi level originates from the t_{1u} and e_u orbitals, which are formed by the d orbital hybridizations between two Co atoms sitting in different sublattices in a unit cell. Numerous other studies have also been performed using DFT calculations.[39–44]

However, how to deal with correlation effects is a critical issue in the DFT study of a Heusler compound. The standard DFT calculations based on mean-field approximations, such as LSDA and generalized gradient approximation (GGA), often fail to predict the *true* ground-state electronic structures due to the presence of d orbital localization in the vicinity of transition metal atoms, making the many-body effect problematic. Various approaches introducing the many-body effect into the DFT scheme have been proposed to recover the correlation problem being missed in LSDA and GGA, *e.g.*, dynamical mean field theory (DMFT),[45,46] hybrid-type PBE0 functional,[47] GW approximation,[48,49] and the DFT+U method.[50,51] However, the obtained electronic structures strongly depend on the employed method. For example, in Co_2MnSi, the LDSA+DMFT calculations, where the dynamical correlation effect such as the spin-flip term is considered quantitatively, were performed on the basis of the linear muffin-tin orbital (LMTO) method[52] and Korringa–Kohn–Rostoker (KKR) method.[53] The former indicates that the Fermi energy is found at the conduction edge of the minority state, while the latter indicates that it is found at the valence edge. The calculation using the hybrid PBE0 functional also shows that the Fermi level locates at the valence top with a very big HM gap of $\sim$2 eV.[54] The GW calculation,[55] where the electronic self-energy correction is included by many-body perturbation theory, predicts that the Fermi energy lies between the valence and conduction bands of the minority state. For these approaches, the huge computational cost is also a serious problem; applying it to the MTJ model for properties including interfacial magnetocrystalline anisotropy and spin-dependent transport may be difficult. On the other hand, the DFT+U method,[50,51] in which parametrized on-site coulomb (U) and exchange (J) interactions for d-orbitals are introduced in the manner of the Hubbard model,[56,57] is a suitable approach on a practical level. Because of the efficient calculation cost, the DFT+U method can be applied to not only simple bulk materials but also large and realistic systems.

The suitable values of U and J for the DFT+U method are unknown; they depend on the atomic species and surroundings of the atom. A linear response (LR) approach[58,59] is an advanced way to determine the correlation terms theoretically and to exclude the *ad hoc* selection of the parameter values. The $+U$ values at respective localized atom sites can be evaluated with low computational costs using the response function of charge density obtained from the standard LSDA or GGA potential. This method has been applied to various correlated systems and succeeded in describing the ground state accurately.[58–65] A recent study has also reported that the parameters are not transferable among different calculation methods due to non-negligible dependence on computational setups even in theoretically determined values.[58] This implies that the optimal correlation parameters for the system of interest must be estimated by the method used for the calculation; however, the application of this LR-based DFT+U method to Heusler compounds has been limited to structural phase transitions.[66]

In the present work, electronic band calculations based on the DFT+U method are carried out for an $L2_1$ Co-based full Heusler alloy to address these issues. Focusing on the typical model Co_2MnSi, we argue the importance of correlation correction in the alloy and the fundamental electronic structure for clarifying the origin of the minority HM gap. The LR calculations obtain a reasonable correlation parameter for the Y site (Y = Mn in Co_2MnSi) and this correction plays an important role for correlated electrons. On the other hand, the correlation for the Co site is unexpectedly overestimated, and thus, the obtained results are misdirected to a rather unphysical ground state. The failure for this unreliable parameter of Co arises from the fact that the 3d electrons of the Co site behave in an itinerant fashion in the alloy, which means that the mean-field approximations such as LSDA and GGA are enough to describe

the electronic structure of the Co site with high accuracy. We also revealed an important d-orbital hybridization between Co and Mn that mainly dominates the minority HM gap. The energy diagram proposed in this study suggests that the HM gap is tunable by a selected Y atom and/or mixing several elements into the Y site. The results obtained from the LR-based DFT+U method, where the determined correlation parameter is incorporated into only the strongly correlated Y site, are consistent with the experimental observations. Moreover, this methodology is superior to the standard GGA calculation, especially in terms of electronic and magnetic properties. This study is further extended to the other ternary Co_2YSi and quaternary $Co_2(Y_x,Mn_{1-x})Si$, where some Mn atoms are substituted with 3d transition metal Y (Y = Ti, V, Cr, and Fe) to explore the potential for the HM ferromagnet with a wide band gap. The systematical calculations indicate that the ternary alloys are found to be ordinary ferromagnets, whose minority bands do not have a finite gap at the Fermi energy, but quaternary Co_2(Ti,Mn)Si, Co_2(V,Mn)Si, and Co_2(Fe,Mn)Si alloys have the potential to be an HM material if the composition of Y is appropriately selected.

This paper is organized as follows. In Section 2, the model and computational details are described, and the LR calculation procedures for the correlation parameters are overviewed. Section 3 revisits Co_2MnSi. The effective on-site coulomb interaction parameters for Co and Mn are first computed from the LR theory (Section 3.1). The structural parameters, including the equilibrium lattice constant and bulk modulus, are evaluated by standard GGA and GGA+U schemes with LR-determined parameters in Section 3.2. Using the obtained lattice constant, the electronic structures are investigated to clarify the HM origin within the GGA framework (Section 3.3). The understanding of a fundamental band structure in GGA is essential for discussing the effects of correlation correction on Mn and Co, which is given in Section 3.4. The LR-based DFT+U calculations for electronic and magnetic structures are presented and compared with previous theories and experiments in Section 3.5. Finally, in Section 4, systematical results for the other ternary and quaternary compounds are discussed and promising materials for HM ferromagnets are proposed.

2 Model and method

The full Heusler Co_2MnSi compound with the $L2_1$ structure has $Fm\bar{3}m$ (O_h) symmetry (space group no. 225). For the modeling, a fcc-primitive cell that contains two Co atoms sitting at the Wyckoff position (1/4, 1/4, 1/4) (multiplicity with Wyckoff letter is 8c), one Mn atom at (1/2, 1/2, 1/2) (4b), and one sp-element Si at (0, 0, 0) (4a) was prepared (a conventional unit cell is shown in Fig. 1(a)). The detailed crystal structures for the ternary system Co_2YSi, where Mn is replaced with Y of Ti, V, Cr, or Fe, and quaternary Co_2(Y,Mn)Si, where some Mn atoms are substituted with Y, are described in Section 4.

The self-consistent DFT calculations were performed *via* the *ab initio* package of Quantum-ESPRESSO[67] by implementing the ultra-soft pseudopotentials parametrized by the scheme of Rappe, Rabe, Kaxiras, and Joannopoulos[68,69] that were taken from the PS Library. The plane wave basis sets for the wave function and charge density had cutoff energies of 40 and 400 Ry, respectively. The self-consistent procedures were achieved until the iterative total energy difference became less than the convergence criterion of 10^{-8} Ry, by using the Monkhorst–Pack special k-point mesh[70] of 16 × 16 × 16 in the first Brillouin zone by the Methfessel–Paxton[71] smearing method with a broadening parameter of 0.02 Ry. Previous works discussed the role of spin–orbit coupling (SOC) in the Heusler alloys and found that the orbital magnetic moment induced by the SOC is completely quenched.[42,72] It is also reported that although a non-vanishing DOS appears in the minority gap by the effect of SOC, the reduction on P is very small.[72–74] In present work, therefore, the SOC is not incorporated into all our calculations. Importantly, it is expected that the wide-gap half-metallic Heusler alloy is robust against the non-vanishing DOS arising from the SOC.

The GGA functional formulated by Perdew, Burke, and Ernzerhof[75] was used for the exchange-correlation term. For the DFT+U method, the choice of "double-counting" correction term is also crucial to subtract the electron coulomb energy that is already included in the LSDA or GGA functional. This correction is conceptually desired to be the same energy contribution as that defined in LSDA or GGA. So far, however, an appropriate prescription for the double-counting term has not been established, but the so-called fully localized limit (FLL),[76–79] which is also referred as the atomic limit (AL), and around mean-field (AMF)[50,78] approaches are mostly used. The former functional favors integer electron occupation numbers at a localized site, and thus, might be useful for strongly correlated materials such as insulating oxide systems. The latter might be useful for an intermediate between strongly correlated and itinerant materials. It is still under debate which of the two

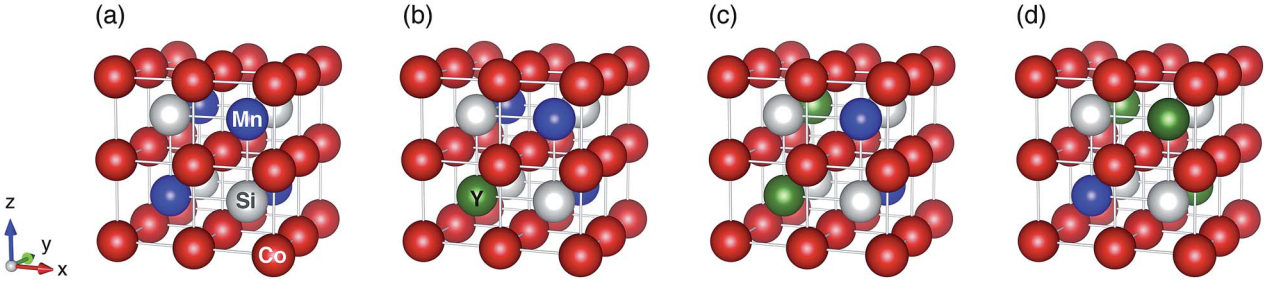

Fig. 1 $L2_1$ symmetric crystal structures for (a) ternary Co_2MnSi, (b) quaternary $Co_2(Y_{0.25},Mn_{0.75})Si$, (c) $Co_2(Y_{0.50},Mn_{0.50})Si$, and (d) $Co_2(Y_{0.75},Mn_{0.25})Si$. Red, blue, white, and green circles indicate Co, Mn, Si, and Y atoms, respectively, where Y is the 3d transition metal atom of Ti, V, Cr, or Fe.

functionals is a proper approach for Heusler compounds.[80] In this study, the double-counting functional incorporated in the simplified rotationally invariant form,[59,81,82] which is equivalent to the FLL approach but $J = 0$ (or approximately $U_{\mathrm{eff}} = U - J$, where U_{eff} stands for the effective on-site coulomb interaction), was employed. We expect that this approach can easily address the underlying physics of correlated electronic structures, compared to AMF, because the electron-localization limit in FLL corresponds to the concept of the Hubbard model; thus, the scaling of U_{eff} can be simply understood as the strength of electron correlation. The U_{eff} is computed within the LR theory[58,59] for all transition metal atoms, where we assume that the coulomb interaction is more dominant than the exchange at localized electron sites.

In the framework of LR theory,[59] the on-site parameter for an atom α, $U_{\mathrm{eff}}^{\mathrm{LR}(\alpha)}$, is evaluated from the second derivatives of the total energy functionals as

$$U_{\mathrm{eff}}^{\mathrm{LR}(\alpha)} = \frac{\partial^2 E^{\mathrm{SCF}}\left[\{q_\alpha\}\right]}{\partial {q_\alpha}^2} - \frac{\partial^2 E^{\mathrm{KS}}\left[\{q_\alpha\}\right]}{\partial {q_\alpha}^2}. \quad (1)$$

The total energies E^{SCF} and E^{KS} correspond to interacting (fully screened) and non-interacting systems. The second term in eqn (1) is necessary to subtract unphysical contributions in the total energy,[83–85] which are caused by the conventional exchange-correlation functionals (LSDA and GGA), where the total energy has a curvature for non-integer occupation q_α and often misdirects to incorrect energy minima. The total energy derivatives are calculated using the constrained DFT approach:

$$E^{\mathrm{i}}\left[\{q_\alpha\}\right] = \min_{n(\boldsymbol{r}),\mu_\alpha}\left\{E^{\mathrm{i}}_{\mathrm{GGA}}\left[n(\boldsymbol{r})\right] + \sum_\alpha \mu_\alpha(n_\alpha - q_\alpha)\right\}, \quad (2)$$

where

$$\frac{\partial}{\partial q_\alpha}E^{\mathrm{i}}\left[\{q_\alpha\}\right] = -\mu_\alpha, \quad \frac{\partial^2}{\partial {q_\alpha}^2}E^{\mathrm{i}}\left[\{q_\alpha\}\right] = -\frac{\partial \mu_\alpha}{\partial q_\alpha}. \quad (3)$$

The Lagrange multiplier μ_α is a local perturbation potential that constrains the occupations n_α (i = SCF, KS). In practice, eqn (2) is transformed into a tractable representation where the constraint fields are treated as independent variables by Legendre transformation and the variations of n_α with respect to μ_α are evaluated.[59] Using nonlocal linear response matrices

$$(\chi_{\mathrm{SCF}})_{\beta\alpha} = \frac{\partial n_\beta}{\partial \mu_\alpha}, \quad (\chi_{\mathrm{KS}})_{\beta\alpha} = \frac{\partial n_\beta^{\mathrm{KS}}}{\partial \mu_\alpha}, \quad (4)$$

eqn (1) is rewritten to obtain $U_{\mathrm{eff}}^{\mathrm{LR}(\alpha)}$ as

$$U_{\mathrm{eff}}^{\mathrm{LR}(\alpha)} = ({\chi_{\mathrm{KS}}}^{-1} - {\chi_{\mathrm{SCF}}}^{-1})_{\alpha\alpha}. \quad (5)$$

The matrix elements of the response matrices are numerically computed; χ_{SCF} is obtained from the self-consistent (interacting) calculations under the applied local potential μ_α and χ_{KS} is obtained from the first iteration in a self-consistent cycle after the end of GGA ground-state calculations – the latter is occupation changes that arise from noninteracting hybridization due to μ_α. The LR approach, in principle, requires a response of the electron occupations to the perturbed potentials at a single site in an infinite crystal environment for an accurate U_{eff} evaluation, where all artifacts due to the periodic boundary conditions are excluded.[58,59]

3 Revisiting Co_2MnSi

3.1 LR-calculation for effective on-site coulomb interaction parameter

The LR calculations are performed to determine the correlation $U_{\mathrm{eff}}^{\mathrm{LR}(\alpha)}$ parameters. The response functions of eqn (4) are evaluated numerically from the gradient of the 3d electron occupation numbers with regard to the perturbed potential μ_α, which constrains the electrons of Co or Mn in the Co_2MnSi alloy. For the LR calculations, the experimental lattice constant $a_{\mathrm{Expt.}} = 5.645$ Å (ref. 18) is employed. As presented in Fig. 2(a) and (b), the occupations' variation of the KS term in the $1 \times 1 \times 1$ primitive cell is slightly off the others ($n \times n \times n$ cells where $n = 2, 3, 4$), although the SCF term does not change much (the plotted data are overlapping and the variations for different supercell sizes may not be visible from these figures). The calculated $U_{\mathrm{eff}}^{\mathrm{LR}}$ value is plotted as a function of the number of atoms per cell in Fig. 2(c). We find a $3 \times 3 \times 3$ fcc supercell including 108 atoms is practically large enough to obtain well-converged parameters, meaning that the environment of the infinite crystal structure is well-reproduced. The obtained values result in $U_{\mathrm{eff}}^{\mathrm{LR(Mn)}} = 3.535$ and $U_{\mathrm{eff}}^{\mathrm{LR(Co)}} = 6.570$ eV for Mn and Co, respectively.

The correlation parameter for Co is unexpectedly higher than the typically used empirical values, for instance, the $U_{\mathrm{eff}}(=U-J)$ of 2.5 eV in full-potential (FP)-LMTO[86] and that of 2.1 eV in KKR[53] calculations. The constrained random phase approximation (cRPA) approach[87] determines a parameter value similar to that determined in our study for Mn (3.07 eV), but

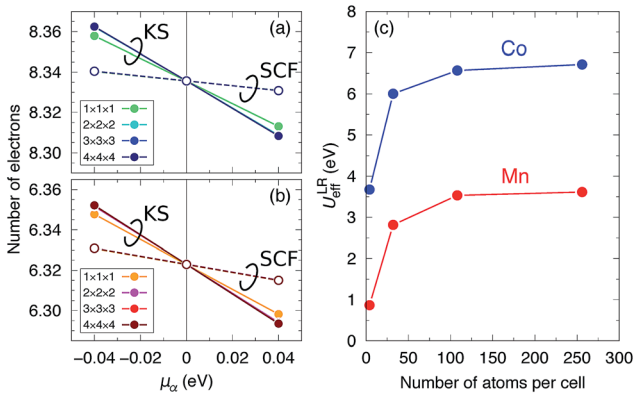

Fig. 2 Variation of the occupied 3d electron numbers on the (a) Co and (b) Mn sites as a function of the applied perturbation potential μ_α in $n \times n \times n$ supercell Co_2MnSi ($n = 1, 2, 3, 4$). Solid lines indicate the KS calculation terms and dashed ones indicate the SCF terms. (c) The $U_{\mathrm{eff}}^{\mathrm{LR}}$ value dependence on the number of atoms per cell for Co (blue) and Mn (red).

determines a value of almost half our LR result for Co (3.28 eV). Table 1 summarizes the numerical data of the d occupations (n_α) and the changes (Δn_α) induced by μ_α in the LR calculations for α atoms (α = Mn and Co). As defined in eqn (4) and (5), the $U_{\text{eff}}^{\text{LR}}$ is difference of the inversions of electron occupations' responses with respect to the applied potential shift μ_α between the KS and SCF terms. For both the α = Mn and Co cases, the absolute values of Δn_α in SCF are smaller than those in KS by one order of magnitude, so the inverted response function $\left(\chi^{-1} \propto \frac{1}{\Delta n_\alpha}\right)$ of SCF becomes a main factor in the computed correlation parameters. We also find that, for the SCF term, Δn_{Co} is small compared to Δn_{Mn}. Therefore, the unreasonably overestimated parameter for Co originates from the difference in Δn_{Co} of the SCF term. Using the diagonal matrix elements of ${\chi_{\text{KS}}}^{-1}$ and ${\chi_{\text{SCF}}}^{-1}$ in eqn (5), the parameter for Co is calculated as $U_{\text{eff}}^{\text{LR(Co)}} = -1.10114 - (-7.67152) = 6.570$ eV. For Mn, $U_{\text{eff}}^{\text{LR(Mn)}} = -0.98733 - (-4.52196) = 3.535$ eV is obtained, where the inverted KS response function's contribution (the first term) is almost the same as in the $U_{\text{eff}}^{\text{LR(Co)}}$ case, while the SCF one (the second term) is significantly different.

From the above discussion, we conclude that the overestimation of $U_{\text{eff}}^{\text{LR}}$ for the Co site arises from the fact that the charge density response of Co is insensitive compared to Mn or is still insufficient to evaluate the parameters through the SCF iteration cycles under the applied potential shift.[88] This can be attributed to the delocalized electronic structures of Co compared to Mn, which originate from the fact that the Co d orbital distribution is spatially-spread due to the d orbital hybridization with first (Mn) and second (Co) neighboring atoms, whereas the Mn d orbital distribution is spatially-narrow due to the d hybridization with only first (Co) neighboring atoms, as discussed in Section 3.3. The localized characters of the Co electronic states compared to those of Mn are consistent with the fact that the spin magnetic moment of Co (1.05 μ_{B}) is much smaller than that of Mn (2.95 μ_{B}). Recently, an extended LR theory[89] has been proposed to overcome the insufficiency of response of charge density; the second response of charge density is additionally included, which is required for complete cancelation of the electron–electron coulomb interaction (Hartree energy) term changed by the external potential ($\mu_\alpha \neq 0$), which might be canceled incompletely in the current LR calculation. In the present study, the DFT+U method incorporated by the FLL formalism is used, but another approach for solving the failure in estimating $U_{\text{eff}}^{\text{LR}}$ for a weakly correlated Co site might be the use of the AMF approximation[50,78] or a *hybrid* approach,[90] where the AMF and FLL approximations are linearly interpolated.

Table 1 Numerical data of LR calculations for $U_{\text{eff}}^{\text{LR}(\alpha)}$ parameters (α = Mn or Co): d occupation numbers (n_α) and changes (Δn_α) of the on-site α atom from the neutral state (μ_α = 0 eV) for the KS and SCF terms when the perturbed potential is applied to the on-site α atom ($\mu_\alpha \neq$ 0 eV). The results are obtained from the 3 × 3 × 3 supercell, in which the well-converged parameters are computed

		KS		SCF	
	μ_α (eV)	n_α	Δn_α	n_α	Δn_α
Mn	−0.04	6.35202	0.02908	6.33086	0.00792
	0.00	6.32294	0.00000	6.32294	0.00000
	0.04	6.29357	−0.02937	6.31500	−0.00794
Co	−0.04	8.36249	0.02682	8.34047	0.00480
	0.00	8.33567	0.00000	8.33567	0.00000
	0.04	8.30830	−0.02737	8.33085	−0.00482

3.2 Structural properties

Here, we consider three schemes of LR-based DFT+U calculations, in addition to the standard GGA: the determined $U_{\text{eff}}^{\text{LR}}$ values are applied to only Mn (referred as GGA+$U_{\text{Mn}}^{\text{LR}}$) or Co (GGA+$U_{\text{Co}}^{\text{LR}}$) and to both of them (GGA+$U_{\text{Mn,Co}}^{\text{LR}}$). First, the GGA calculations are performed to evaluate the equilibrium lattice constant. The total energies at different volume sizes of primitive cell are obtained as shown in Fig. 3(a). The energy minimum is searched by energy fitting to the Murnaghan equation of states[91] as a function of volume V,

$$E(V) = E_0 + \frac{B_0 V}{B_0'}\left[\frac{1}{B_0' - 1}\left(\frac{V_0}{V}\right)^{B_0'} + 1\right] - \frac{B_0}{B_0' - 1}V_0, \quad (6)$$

where E_0 is the ground-state total energy at equilibrium volume V_0, B_0 is the bulk modulus, and B_0' is the pressure derivative of the bulk modulus. The obtained lattice constant is 5.639 Å, which agrees with the experimental value.[18] The error value

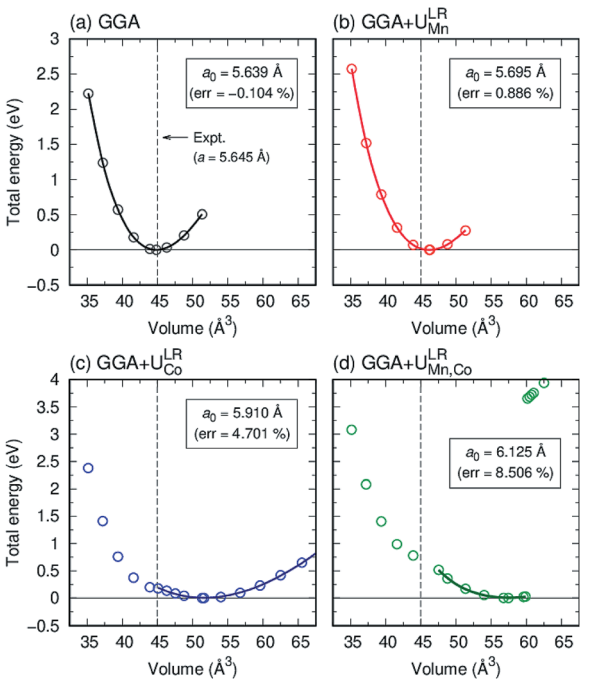

Fig. 3 Total energy as a function of volume for Co_2MnSi from (a) GGA, (b) GGA+$U_{\text{Mn}}^{\text{LR}}$ (c) GGA+$U_{\text{Co}}^{\text{LR}}$, and (d) GGA+$U_{\text{Mn,Co}}^{\text{LR}}$. Open circles are obtained from first principles and solid lines from Murnaghan fitting, which determines the equilibrium lattice constant a_0, as shown in the inset. The error from the experiment is also shown in the parentheses. The experimental value is plotted by a dashed (black) line.

between the calculated lattice constant a_0 and experiment, defined as $(a_0 - a_{\text{Expt.}})/a_{\text{Expt.}} \times 100$ (%), is only −0.104%. In the GGA+$U_{\text{eff}}^{\text{LR}}$ case, the obtained lattice constant of 5.695 Å is similar to the GGA result and the error from the experiment is less than 1% (0.866%), as shown in Fig. 3(b). On the other hand, a_0 is significantly overestimated by the errors of 4.701 and 8.506% in the GGA+$U_{\text{Co}}^{\text{LR}}$ and GGA+$U_{\text{Mn,Co}}^{\text{LR}}$ cases. Fig. 3(c) shows a local energy minimum around the experimental value but the global minimum is found at 51.62 Å^3, corresponding to $a_0 = 5.910$ Å. Note also that in the GGA+$U_{\text{Mn,Co}}^{\text{LR}}$ scheme (Fig. 3(d)), a jump of total energy change around the volume of ∼60 Å^3 occurs due to a magnetic phase transition, but we confirm that an energy minimum, corresponding to $a_0 = 6.125$ Å, exists at less than the volume where this magnetic transition is induced.

We present bulk modulus B_0 and its pressure derivative B_0' in Table 2, through comparisons of theoretical literature.[42,92–95] Among the previous reports, the B_0 of LSDA is greater than that of GGA. Our GGA result is almost similar to the reported values in B_0 and B_0', while the GGA+$U_{\text{Mn}}^{\text{LR}}$ result is slightly smaller in B_0. On the other hand, the B_0 calculated by the GGA+$U_{\text{Co}}^{\text{LR}}$ and GGA+$U_{\text{Mn,Co}}^{\text{LR}}$ methods is one order of magnitude smaller than the other calculations. Because the experimental data of the bulk modulus and its derivative are not available for Co_2MnSi at this moment, we cannot conclude the validity of our method. However, at least focusing on the lattice constant, these results indicate that the introduction of $U_{\text{eff}}^{\text{LR}}$ to the Mn atom tends to obtain a reasonable result, as well as GGA, from the comparison with experiments, while the inclusion of $U_{\text{eff}}^{\text{LR}}$ to Co fails to evaluate the a_0 of Co_2MnSi.

3.3 Origin of half-metallicity

As mentioned in Section 2, the full Heusler alloy of $L2_1$ structure belongs to the octahedral (O_h) space group symmetry. In this *whole-crystal* symmetry, we first focus on the Co lattice by ignoring the first-neighboring Mn and Si atoms. The lattice is assumed to be a simple cubic composed by the second-neighboring Co at different sublattices in the primitive cell, which leads to the Co sitting at O_h site symmetry. Secondly, our focus turns to the tetrahedral (T_d) site symmetry. Neglecting the chemical atomic species, every atom forms a bcc lattice structure and is surrounded by a tetrahedral environment. The hybridization diagram of atomic orbital energy is discussed by following these two steps. Note that, to avoid confusion regarding the notations, the symmetric characters of the atomic orbitals are unified using only representations for the O_h site symmetry, which corresponds to the space group of the $L2_1$ full Heusler compound, as done in previous research.[38]

We again start with the results of the standard GGA calculations to discuss the underlying electronic structure of Co_2MnSi. Fig. 4(a) shows the band structures for the minority spin states projected into the Co $e_{g(u)}$ (d_{z^2}, $d_{x^2-y^2}$) and $t_{2g(1u)}$ (d_{xz}, d_{yz}, d_{xy}), Mn e_g (d_{z^2}, $d_{x^2-y^2}$) and t_{2g} (d_{xz}, d_{yz}, d_{xy}), and Si t_{1u} (p_x, p_y, p_z) orbitals. The lattice constant is set to the theoretically obtained value of 5.639 Å. The d states of Co and Mn are visible around the Fermi energy, while the Si t_{1u} state can be seen only very far from the Fermi energy. To discuss the orbital hybridization mechanism, the eigenstates at the Γ point in the Brillouin zone are focused on. At 0.4 eV above the Fermi energy, the Co e_u^* state (this state is an anti-bonding state as discussed in the next paragraph) appears but the other orbital components are not included in these eigenstates, which means that Co e_u^* does not hybridize with the other atomic orbitals. We can find t_{2g} hybridization between Co and Mn that forms a bonding Mn t_{2g} state at −1.4 eV and an anti-bonding Co t_{2g}^* at 0.3 eV. As a result, a minority band gap originates from the anti-bonding t_{2g}^* and non-bonding e_u^* states of the Co atom. Another essential orbital hybridization is found in the t_{1u} symmetry character between Co and Si. The eigenstate components of Co and Si exist at energy levels of 3.8 and 3.9 eV, respectively, so that the Co and Si atoms contribute to the anti-bonding state (t_{1u}^*) and to the bonding state (t_{1u}), respectively. We do not mention the e_g hybridization between Co and Mn as it has already been discussed previously.[38]

Fig. 4(b) presents an energy diagram of Co atoms with O_h site symmetry. Due to the crystal field, the e_g and t_{2g} orbitals are formed and hybridize with the same character orbitals of Co at the other site. These hybridizations arise from the bonding states of e_g and t_{2g} orbitals and anti-bonding states of e_u^* and t_{1u}^* orbitals. The t_{2g} orbital hybridization, including $d_{xz} - d_{xz}$, $d_{yz} - d_{yz}$, and $d_{xy} - d_{xy}$, is expected to form a π-like bonding in the O_h atomic positions, and the e_g hybridization, including $d_{z^2} - d_{z^2}$ and $d_{x^2-y^2} - d_{x^2-y^2}$, is expected to form a σ-like bonding, whose orbital coupling is stronger than that of π-like bonding. Accordingly, the energy gap between bonding e_g and anti-

Table 2 Structural parameters of lattice constant a_0, bulk modulus B_0, and its pressure derivative B_0' for Co_2MnSi. The $U_{\text{eff}}^{\text{LR}}$ values determined by the LR approach are employed in the present study: $U_{\text{eff}}^{\text{LR(Mn)}} = 3.535$ eV for GGA+$U_{\text{Mn}}^{\text{LR}}$, $U_{\text{eff}}^{\text{LR(Co)}} = 6.570$ eV for GGA+$U_{\text{Co}}^{\text{LR}}$, and both for GGA+$U_{\text{Mn,Co}}^{\text{LR}}$

		a_0 (Å)	B_0 (GPa)	B_0'
Present work	GGA	5.639	217.63	4.30
	GGA+$U_{\text{Mn}}^{\text{LR}}$	5.659	186.29	4.41
	GGA+$U_{\text{Co}}^{\text{LR}}$	5.910	65.40	1.25
	GGA+$U_{\text{Mn,Co}}^{\text{LR}}$	6.125	60.70	5.74
Theory	LSDA	5.54[a]	258.0[a]	
	GGA	5.643[b], 5.633[c], 5.639[d], 5.642[e]	226[b], 212.8[c], 214[d], 240.89[e]	4.680[c], 4.674[d], 4.983[e]
Experiment		5.645[f]		

[a] Ref. 92. [b] Ref. 42. [c] Ref. 93. [d] Ref. 94. [e] Ref. 95. [f] Ref. 18.

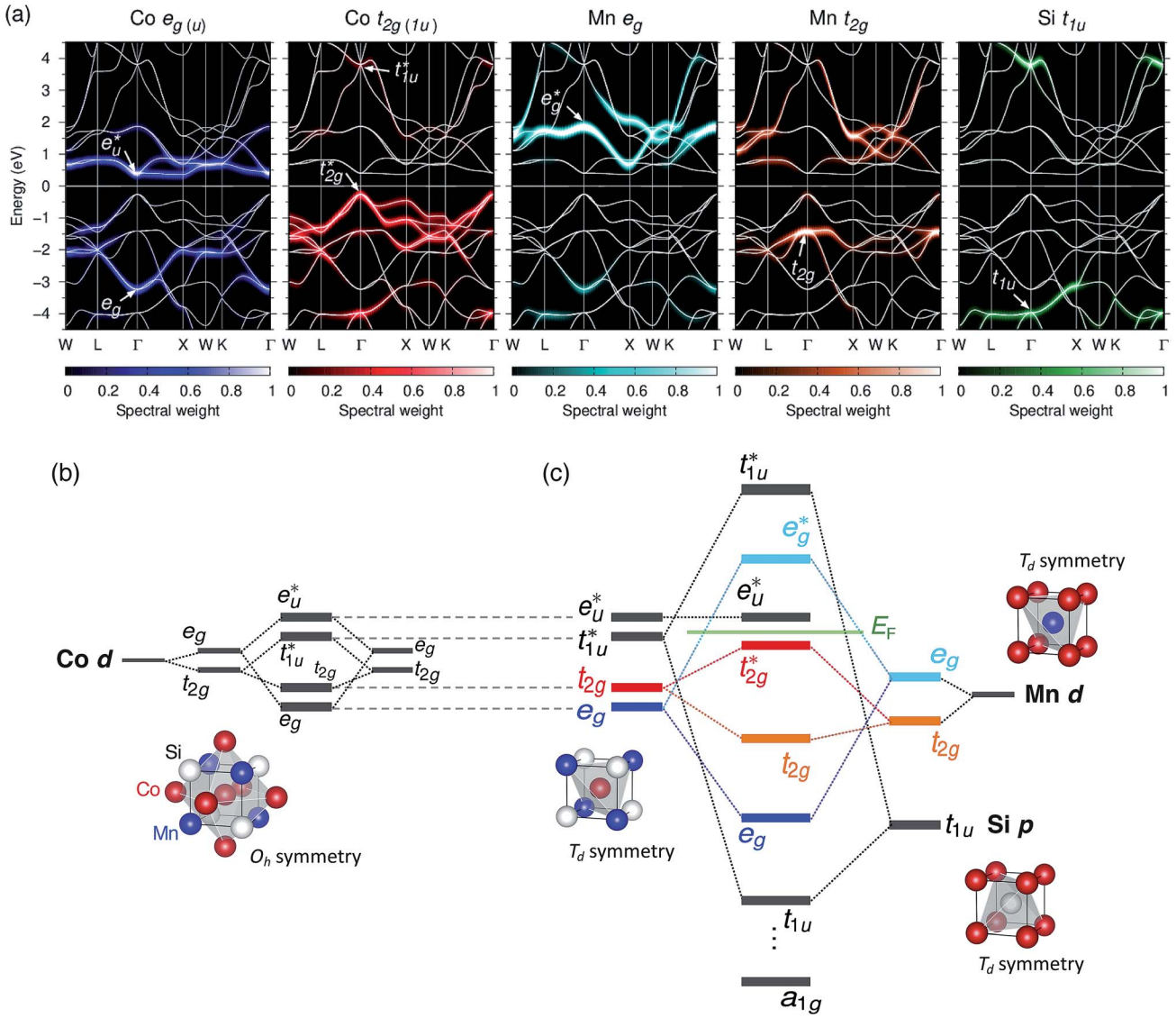

Fig. 4 (a) Projected band structures for minority spin in Co_2MnSi. The orbital-component spectral weights of $e_{g(u)}$ (blue) and $t_{2g(1u)}$ (red) symmetries for Co d orbitals, e_g (skyblue) and t_{2g} (orange) for Mn d, and t_{1u} (green) for Si p are shown by the colormap. The total band structure of the minority spin is also plotted by a white solid line. The Fermi energy is set to zero. Minority-spin-state atomic-orbital energy diagrams of (b) hybridizations of d orbitals between two Co atoms at different sublattices in O_h site symmetry and (c) hybridizations among Co–Co d, Mn d, and Si p in T_d site symmetry, where a_{1g} corresponds to a Si s orbital which does not appear in the projected bands given in (a). Note the orbital symmetry characters are represented under the O_h site symmetry throughout the diagram: representations of d – e (d_{z^2}, $d_{x^2-y^2}$), –t_2 (d_{xz}, d_{yz}, d_{xy}), and p – t_2 (p_x, p_y, p_z) states in T_d site symmetry can be transformed into those of e_g, t_{2g}, and t_{1u} states in O_h site symmetry, respectively.

bonding e_u^* states arising from e_g hybridization becomes wide compared to that from the bonding t_{2g} and anti-bonding t_{1u}^* states from t_{2g} hybridization.

Next, the orbital interactions between the first-neighboring atoms are discussed by focusing on T_d site symmetry. Before that, we mention here the correlation between the O_h and T_d site symmetries and the possibility of atomic orbitals hybridizing. The T_d site symmetry, which is a subgroup of the O_h site symmetry, has the same irreducible representations as the O_h site symmetry except for an absence (presence) of inversion symmetry in T_d (O_h) site symmetry. The Co–Co d orbital's character in the O_h site symmetry can be transformed into the T_d notation; the doublet e_g and e_u^* orbitals in O_h are represented as the e character in T_d, and the triplet t_{2g} and t_{1u}^* orbitals as t_2 character. The T_d site symmetry also gives the e (d_{z^2}, $d_{x^2-y^2}$) and t_2 (d_{xz}, d_{yz}, d_{xy}) characters for Mn and t_2 (p_x, p_y, p_z) for Si. These augments allow Co–Mn and Co–Si to interact in the atomic orbitals in T_d site symmetry, *i.e.*, t_{2g} orbital hybridization of Co–Mn and t_{1u} orbital hybridization of Co–Si in O_h site symmetry.

Fig. 4(c) illustrates the possible energy diagram between Co–Co and Mn or Si. The a_{1g} orbital corresponds to the Si s orbital, which does not appear in the band structure of Fig. 4(a) because the energy level is very low. The anti-bonding Co t_{2g}^* state dominates the highest orbital state in the valence band, which

hybridizes with the bonding Mn t_{2g}. The Co t_{1u}^{*} is pushed up to quite a higher energy through hybridization with the Si t_{1u} (p) orbital and the non-bonding Co e_u^{*} is left at above the Fermi level. This energy diagram, thus, suggests that the main contributions to constructing the minority band gap arise from the t_{2g} coupling of Co and Mn atoms and the t_{1u} orbital of Co no longer contributes to the gap; this conclusion is different from that of a previous study,[38] where the band gap in the minority state is mostly dominated by Co e_u and t_{1u} orbitals (these orbital characters are used in previous work). Instead, more importantly, our diagram proposes that the HM property and electronic structure near the Fermi level can be tuned by selection of the Y atom and/or a mix of several atoms in the Y site through t_{2g} coupling in $L2_1$ Heusler alloys.

Even though our diagram differs from the previously reported one,[38] the 12 valence electrons for Co_2MnSi are confirmed to occupy three Co t_{2g}^{*}, three Mn t_{2g}, two Co e_g, three Si t_{1u}, and one Si a_{1g} orbitals in the down-spin state. This means our diagram satisfies the well-known Slater–Pauling relation:[38] the magnetic moment of the system, m_{spin}, obeys $m_{spin} = N_{val} - 24$, where N_{val} is the total number of valence electrons. The calculations obtain a total magnetic moment of 5.01 μ_B, which is very close to the integer value expected by the Slater–Pauling rule and in agreement with a previous theory within LSDA[38] and GGA,[42,44] as well as experiments,[96–99] as summarized in Table 3.

Note that the previous study[38] was carried out for Co_2MnGe, where the number of valence electrons is equivalent to that of Co_2MnSi. Thus, Co_2MnGe is confirmed to be similar to Co_2MnSi. The energy diagram obtained from the band structure calculations corresponds to Fig. 4(c) and the integer value of the total spin magnetic moment is calculated (m_{spin} = 5.00 μ_B).

Table 3 Total and atom-resolved magnetic moments (in μ_B) for Co_2MnSi with comparison to present and previous theories as well as experiments. The representations in the present paper are the same as those in Table 2. The first column gives the calculation methods (and types of exchange-correlation functionals in parentheses) for theory and measurement techniques for experiment

	Total	Co	Mn	Si
Present work				
GGA	5.01	1.05	2.95	−0.05
GGA+U_{Mn}^{LR}	5.01	0.72	3.63	−0.08
GGA+U_{Co}^{LR}	6.95	1.88	3.19	−0.09
GGA+$U_{Mn,Co}^{LR}$	8.08	1.94	4.05	−0.06
Theory[a]				
FS-KKR[38] (LSDA)	4.94	1.02	2.97	−0.07
ASA-ASW[44] (GGA)	5.00	0.93	3.21	−0.06
FLAPW[42] (GGA)	5.00	1.06	2.92	−0.04
FP-LMTO[86] (GGA+U^b)	5.00	1.08	2.97	−0.08
MLWF-FLAPW[87] (GGA+U^c)	5.00	1.05	3.01	−0.06
KKR[53] (LSDA+DMFT[d])	4.97			
FLAPW-GW[55] (GGA)	5.00			
Experiment[e]				
Sucksmith[96]	5.07	0.75	3.57	
Ref. 97	5.01			
SQUID[98]	4.97			
SQUID[99]	5.00	0.72	3.34	

[a] FS-KKR: full-potential screened Korringa–Kohn–Rostoker Green's function method; ASA: atomic sphere approximation; ASW: augmented spherical waves method; FLAPW: full-potential linearized augmented plane wave method; FP-LMTO: full-potential liner muffin-tin orbital method; MLWF: maximally localized Wannier functions; GW: GW approximation. [b] The U and J values of 3.5 (5.0) and 1.0 (0.9) eV for Co (Mn), respectively, are chosen to reproduce the total spin magnetic moment observed experimentally. [c] The respective U_{eff} values of 3.28 and 3.07 eV for Co and Mn are determined by cRPA. [d] The U and J values of 3.0 and 0.9 eV, which have been reported as average values of the determined parameters by theory for pure bulk 3d transition metals, are used. [e] Sucksmith: Sucksmith ring-balance measurement by Faraday method; SQUID: superconducting quantum interface device magnetometry.

3.4 Correlation effects on Mn and Co

As mentioned in the introduction, the behaviors of electron localizations are supposed to be different at Co and Mn sites. This fact motivates us to investigate the effects of the correlations for each site. To discuss the influence of +U on the atomic energy diagram, modifications of magnetic moment and band structure are studied by performing DFT+U calculations with varying U_{eff} parameters for Co and Mn atoms *independently*. Here, we refer to the case where the varying U_{eff} is applied to only the Mn (Co) site for the GGA+U_{Mn} (GGA+U_{Co}) representation, where the lattice constant is set to the theoretical value of 5.695 Å (5.910 Å) obtained in Section 3.2.

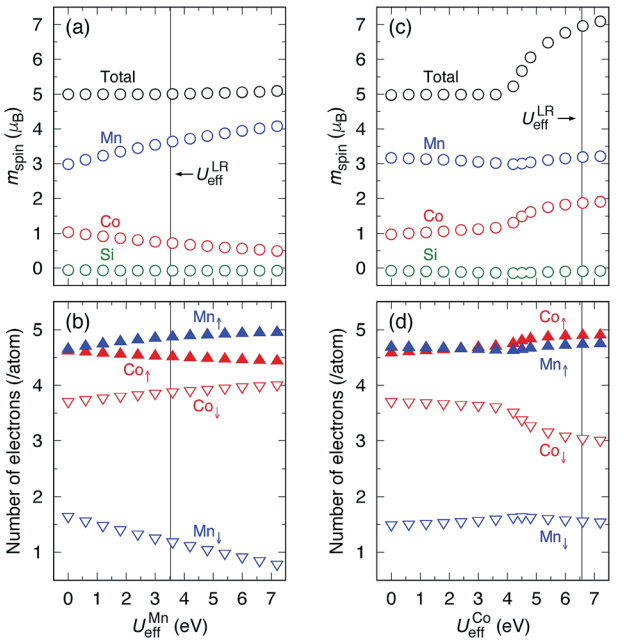

Fig. 5 Dependence of (a) total and atom-resolved spin magnetic moments, m_{spin}, and (b) d orbital occupations with respect to the varying U_{eff}^{Mn} for the GGA+U_{Mn} case. Black, red, blue, and green circles in (a) indicate the total, Co, Mn, and Si, and red and blue up- (down-) pointing triangles in (b) are majority (minority) d occupations for Co and Mn, respectively. The vertical solid line indicates the value of U_{eff}^{LR}. (c and d) Same plots for GGA+U_{eff}^{Co} having the same notations as those in (a and b). U_{eff}^{α} = 0 (α is Mn or Co) indicates the GGA result, where the difference between GGA+U_{Mn} and GGA+U_{Co} comes from the different equilibrium lattice constants.

We first mention the GGA+U_{Mn} case. The total m_{spin} is constant but the Mn (Co) m_{spin} monotonically increases (decreases) when the correlation parameter for Mn, U_{eff}^{Mn}, increases (see Fig. 5(a)). Note that two of the Co atoms exist in the primitive cell, so the variation of the Co m_{spin} is estimated to be twice as great. The increased m_{spin} of Mn arises from a significant reduction in minority spin electron occupations, as shown in Fig. 5(b). This reflects the following behavior: a large +U value intensifies the coulomb interaction contributions and allows electrons to occupy not the same but different orbitals with parallel spins from Pauli exclusion principles and Hund's rule, leading to a gain in kinetic energy.

As the t_{2g} orbitals of Co and Mn change the most noticeably depending on the U_{eff}^{Mn} value, we trace modifications in the band structures of these orbitals. Fig. 6(a) presents the minority spin band structures around the Γ point calculated by standard GGA and the GGA+U_{Mn} with small (U_{eff}^{Mn} = 3 eV) and large (6 eV) parameter values. The GGA results indicate that the anti-bonding Co t_{2g}^{*} is dominant just below the Fermi energy and the bonding Mn t_{2g} is visible at 1.5 eV in a minority state. Interestingly, increasing the U_{eff}^{Mn} value modifies the spectral weights of the minority components; the Mn and Co orbital weights in bonding and anti-bonding states are almost identical at small U_{eff}^{Mn}, but the anti-bonding t_{2g}^{*} becomes dominated by Mn compared to Co and t_{2g}^{*} shifts above the Fermi energy at a large U_{eff}^{Mn}. Schematic diagrams are illustrated in Fig. 6(b) and (c). In the majority spin, the valence Mn t_{2g} atomic orbital is shifted to a lower energy by the U_{eff}^{Mn} effect and the anti-bonding state Co t_{2g}^{*} is drawn to a lower energy by the hybridization with Mn t_{2g}. On the other hand, in the minority state, the energy level of the Mn valence state becomes higher as U_{eff}^{Mn} increases, and the anti-bonding Co t_{2g}^{*} orbital gradually touches the Fermi energy. When the Mn t_{2g} state becomes energetically higher than that of Co at a large U_{eff}^{Mn}, the major component of the anti-bonding t_{2g}^{*} is switched from Co to Mn in minority spin.

Surprisingly, U_{eff}^{Mn} shifts the minority occupied state of Mn *upward* energetically; this shifting is an opposite tendency to the well-known fact of DFT+U study. In general, the +U term opens the band gap with the valence (conduction) state being lower (higher) energy in the insulating and semi-conducting materials regardless of the spin channels. However, ferromagnetic materials, including the Heusler alloy, are different from insulators and semi-conductors because a finite DOS lies at the Fermi energy in ferromagnets. In principle, the total number of valence electrons at each atom site must be preserved even though the +U effect is introduced. Accordingly, the upward shifting in the valence state of the minority Mn d orbital can be understood as follows: the occupations in a spin channel (majority state) increase due to the applied +U effect, but simultaneously, the occupations in the opposite spin (minority state) are reduced to keep the total occupations constant at each atom. This argument is based on the energy diagrams in Fig. 6(b) and (c), and is consistent with the behaviors of the spin magnetic moment and electron occupations at each atomic site

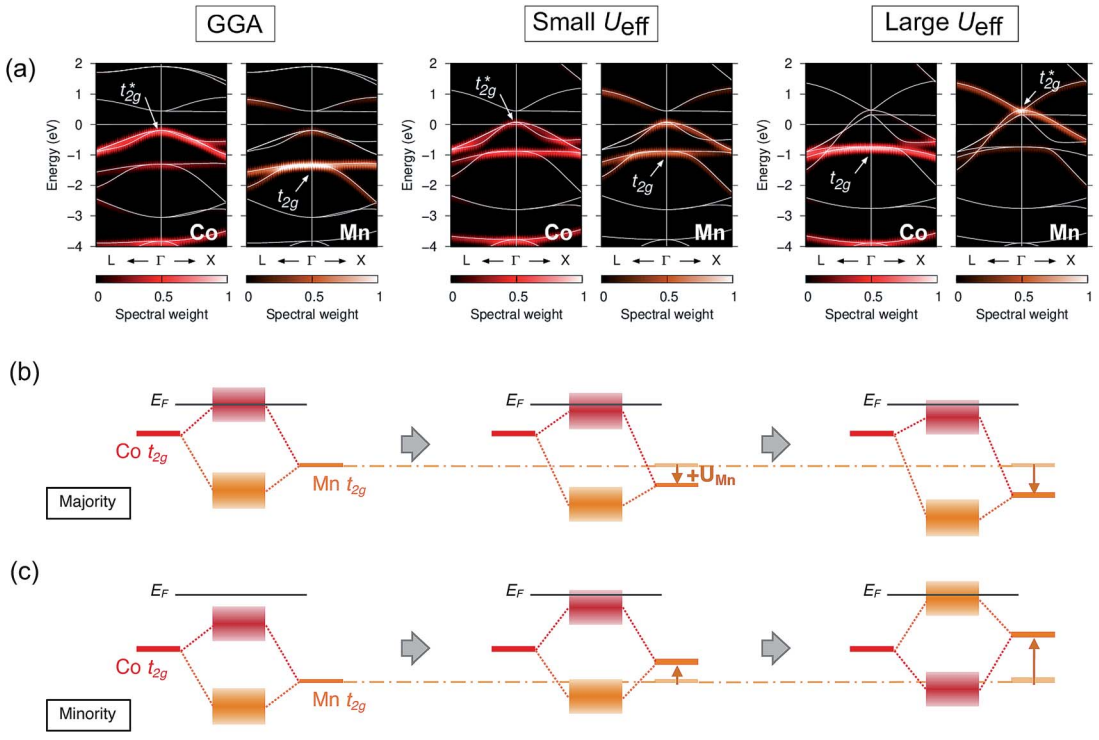

Fig. 6 (a) Dependence of band structures in the minority state on varying +U_{Mn} parameter values, *i.e.*, GGA (U_{eff} = 0 eV for the Mn site), small (3 eV) and large (6 eV), where the projected spectral weights for the Co and Mn t_{2g} states are shown in the left (red) and right (orange) panels, respectively. The Fermi energy is set to zero and the total minority band structure is plotted by a white line. Schematic summary of the changes in atomic orbital hybridizations for (b) majority and (c) minority states. Arrows in (b and c) indicate the energy shift induced by the effect of U_{eff}^{Mn}.

[Fig. 5(a) and (b)]; thus, this scenario can be concluded to be behind the effects of $+U$ on the Mn d orbitals.

Secondly, the GGA+U_{Co} result is considered. In the range of U_{eff}^{Co} less than around 4 eV, the increase in the spin magnetic moment at the Co site is not significant, but it suddenly increases afterward [Fig. 5(c)]. In Fig. 7, the U_{eff}^{Co}-dependent electronic band structures and hybridization behaviors of Co and Mn are summarized. In the valence states, it can be seen that the contribution to the anti-bonding t_{2g}^{*} is switched from Co to Mn [Fig. 7(a)]. In contrast, the anti-bonding e_g^{*} state is switched from Mn to Co [Fig. 7(b)] with increasing U_{eff}^{Co}. The e_u^{*} state in Fig. 7(b) moves to a higher energy on increasing U_{eff}^{Co}, but does not hybridize with Mn.

To understand the behavior of the changing m_{spin} and electron numbers in GGA+U_{Co} in Fig. 5(c) and (d), the possible energy diagrams for the majority and minority states are illustrated in Fig. 7(c) and (d). The majority Co t_{2g}^{*} simply goes to a lower energy on the introduction of U_{eff}^{Co}, so that the Co d spin-up occupation increases and is saturated at larger U_{eff}^{Co} values (~7 eV). For the minority state, the d bands' behaviors of Co and Mn are intricate, but can be understood by going back to the principle view that first attention is paid to the hybridization between Co atoms in different sublattices and then that between the Mn and Co–Co states afterward, as discussed in Section 3.3 and a previous report.[38] The Co d_{z^2} and $d_{x^2-y^2}$ (d_{xz}, d_{yz}, and d_{xy}) orbitals are pushed up (down) due to U_{eff}^{Co}, and

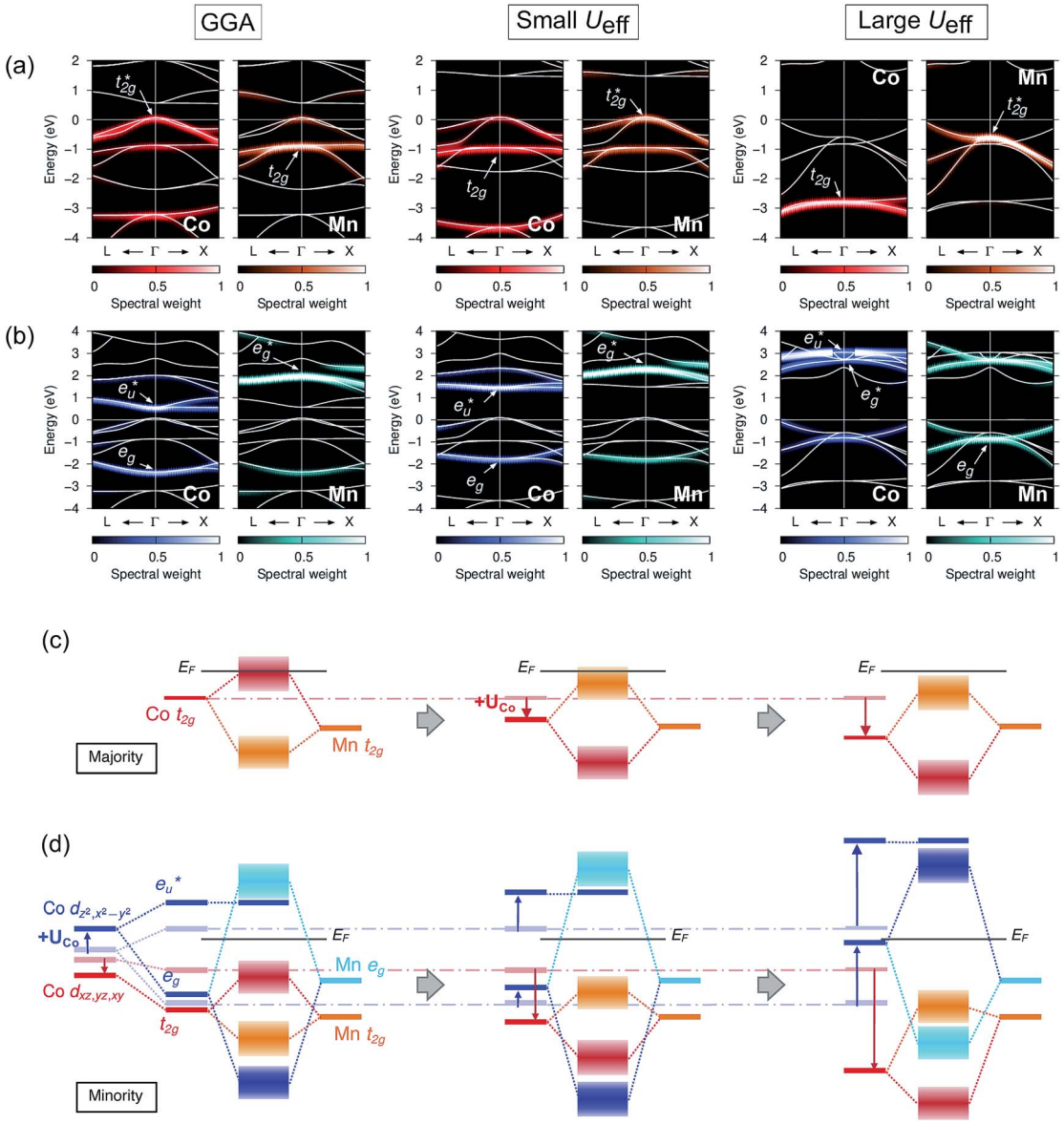

Fig. 7 Dependence of the minority band structures on the varying $+U_{Co}$ parameter values, *i.e.*, GGA (U_{eff} = 0 eV for the Co site), small (3 eV), and large (6 eV), where the projected spectral weights for the (a) Co and Mn t_{2g} states are shown in the left (red) and right (orange) panels, and for the (b) Co and Mn e_g states are shown in the left (blue) and right (sky-blue), respectively. Note that the energy ranges in (a and b) are different. Schematic summary of the changes in atomic orbital hybridizations for (c) majority and (d) minority states. Notation is the same in Fig. 6.

hybridize with the Mn e_g (t_{2g}) state [Fig. 7(d)]. Increasing U_{eff}^{Co} affects the energy gap, and most notably, the Co e_g orbital becomes an un-occupied anti-bonding state at a large U_{eff}^{Co} value, while it is an occupied bonding state at a small U_{eff}^{Co} (see the blue band of the energy diagram in Fig. 7(d)). This event induces a significant reduction in the minority Co occupations [red down-pointing triangle in Fig. 5(d)], resulting in an increase in the total m_{spin} in the range of U_{eff}^{Co} over ~4 eV, as shown by black plots in Fig. 5(c).

From the above discussions, the underlying physics of the correlation effects on the magnetic moment can be addressed from the viewpoint of electronic structure for both the GGA+U_{Mn} and GGA+U_{Co} cases. Thus, the consistency of our energy diagram proposed in Fig. 4(c) is demonstrated successfully.

3.5 Electronic and magnetic properties

We now discuss the electronic and magnetic properties obtained from the band calculations that incorporate the LR-determined correlation parameters (3.535 eV for Mn and 6.570 eV for Co). First, the m_{spin} obtained from the GGA+U_{Mn}^{LR} method is compared with that from the GGA method in Table 3. The value of the total m_{spin} is the same as that of GGA and agrees with previous reports.[53,55,86,87,96–99] On the other hand, regarding the atom-resolved contributions, the results for m_{spin} of Co (0.72 μ_B) and Mn (3.63 μ_B) are not in agreement with GGA and previous calculations, but in good agreement with experiments.[96,99] Thus, the GGA+U_{Mn}^{LR} calculation results are superior to the standard GGA results.

In the GGA-calculated DOS in Fig. 8(a), we can clearly see that the Co d orbital is broad over a wide energy region (from the Fermi energy to 5 eV for the majority state and from 0.5 eV to 4.5 eV for the minority state). Contrarily, the Mn d orbital is relatively localized compared to the Co one and splits into two peaks located around 3 and 1 eV (1.5 and 1.8 eV) in the majority (minority) state, respectively. As expected from Fig. 4(b) and (c), we also confirm the e_u^* and t_{2g}^* orbital characters of the Co d states above and below the Fermi energy, as shown by arrows in Fig. 8(a). The value of spin polarization referred to as P_{DOS} is estimated by $P_{DOS} = \frac{D^{\uparrow}(E_F) - D^{\downarrow}(E_F)}{D^{\uparrow}(E_F) + D^{\downarrow}(E_F)} \times 100\ (\%)$, where $D^{\sigma}(E_F)$ is the DOS of the majority ($\sigma = \uparrow$) or minority ($\sigma = \downarrow$) spin state at the Fermi energy. A 100% P_{DOS} value is obtained, and the energy band gap in the minority spin state $E_{gap}^{\downarrow}$ is around 0.8 eV. The GGA+U_{Mn}^{LR} calculation modifies the DOS from GGA. The energy level of the Mn occupied (unoccupied) states is shifted to a lower (higher) level due to the exchange splitting induced by the $U_{eff}^{LR(Mn)}$ effect. As a result, the valence and conduction edges are dominated mainly by Co d components and only a few Mn d states appear around the Fermi energy. Due to the presence of a few Co d DOSs at the Fermi energy, the half-metallicity is broken but high spin polarization P_{DOS} = 90.5% is obtained.

By contrast, GGA+U_{Co}^{LR} and GGA+$U_{Mn,Co}^{LR}$ seem to fail to obtain the total magnetic moment reasonably consistently with the experimental observations[96,99] because of the overestimated $U_{eff}^{LR(Co)}$ parameters (see Table 3). Fig. 8(c) indicates the fact that the exchange splitting arising from the large $U_{eff}^{LR(Co)}$ induces

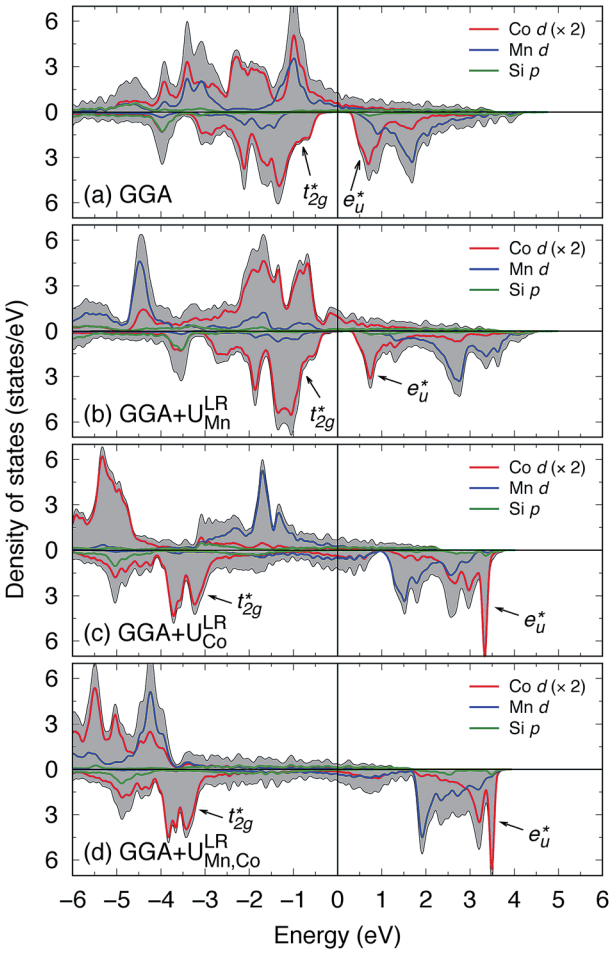

Fig. 8 Local DOS obtained from (a) GGA, (b) GGA+U_{Mn}^{LR}, (c) GGA+U_{Co}^{LR}, and (d) GGA+$U_{Mn,Co}^{LR}$ calculations. Red, blue, and green lines are for Co d, Mn d, and Si p orbitals, and the total DOS is shown by a gray filled area. The orbital characters of the t_{2g}^* and e_u^* states, which originate from Co, are shown with arrows. Note that the local DOS for Co is twice as two Co atoms are included in the primitive cell. The upper (bottom) area in each panel shows the spin-up (-down) state, and the Fermi energy is set to zero.

a fully-occupied Co d state in majority spin states, which leads to a Co m_{spin} of 1.88 μ_B and total m_{spin} of 6.95 μ_B. The energy gap does not appear in the minority channel and the top of the valence states around 2 eV from the Fermi energy is composed of the Mn d orbital of the majority states. Similarly, in the GGA+$U_{Mn,Co}^{LR}$ case, the overestimated value of the total m_{spin} of 8.08 μ_B arises from the fact that the majority electrons of Co and Mn are fully occupied at low energy (4 eV and below) through both $U_{eff}^{LR(Mn)}$ and $U_{eff}^{LR(Co)}$, as shown in Fig. 8(d). In this scheme, the half-metallic electronic structure is broken by a few DOS that are widely broad around the Fermi energy. The spin polarizations are found to be negative and small absolute values: P_{DOS} = −26.97 and 33.82% for the respective GGA+U_{Co}^{LR} and GGA+$U_{Mn,Co}^{LR}$ methods.

From the experimental point of view, hard X-ray photoelectron spectroscopy measurements reported that the valence band structure in the binding energy region from the Fermi energy to

~1.2 eV (corresponding to −1.2 eV in calculated DOS) is mostly contributed to by Co 3d electrons[100] as while the Mn d state does exist in this binding-energy region, the number of electrons is very few compared to Co.[101] Based on the above comparative discussions between our calculations and experiments on the electronic structure and magnetic moment (as well as the equilibrium lattice constant in Section 3.2), we can conclude that the static many-body correlation $+U$ at the Y site (Y = Mn for Co_2MnSi) plays an important role in obtaining ground-state properties that are in good agreement with the experiments. On the other hand, the Co d electrons are rather itinerant in the alloy; thus, the LR approach tends to overestimate the correlation parameter for the Co site, which is not reliable for accurate band calculations. In other words, for the Co site, correlation correction may not be necessary and mean-field approximation (GGA or LSDA) is enough to treat the itinerant Co d electrons. Thus, hereafter, all LR-based DFT+U calculations are performed with $U_{\mathrm{eff}}^{\mathrm{LR}}$ only for the Y site; *i.e.*, correlation correction is excluded for Co. We here explicitly mention that the energy diagram obtained from the GGA+$U_{\mathrm{Mn}}^{\mathrm{LR}}$ calculation corresponds to Fig. 4(b) and (c), which are obtained from the GGA results.

4 Searching for HM materials of other ternary and quaternary alloys

To consider the ternary Co_2Y Si alloys, where Y is changed from Mn to Ti, V, Cr, or Fe atoms, the LR calculations for $U_{\mathrm{eff}}^{\mathrm{LR(Y)}}$ are first carried out using the lattice constants assumed in experiments,[16,18,102] as in the case of Co_2MnSi. To the best of our knowledge, there are no experimental data for Co_2CrSi, so the lattice constant obtained from Murnaghan fitting[91] by the GGA potential is employed for the $U_{\mathrm{eff}}^{\mathrm{LR(Cr)}}$ calculation. In this study the initial magnetization for the SCF calculation is assumed to be the ferromagnetic state in all ternary models. The determined parameters are around 3–4 eV depending on the materials: $U_{\mathrm{eff}}^{\mathrm{LR(Y)}}$ = 2.942, 3.979, 3.169, and 3.922 eV for Co_2TiSi, Co_2VSi, Co_2CrSi, and Co_2FeSi, respectively.[103]

Calculated total DOSs are shown in Fig. 9(a)–(d), and the results for the spin magnetic moments are summarized in Table 4. Co_2TiSi is not HM (P_{DOS} = 25.8%), where the Fermi energy is located at the minority conduction edge state. For Co_2VSi and Co_2CrSi, a few broad minority DOSs are found around the Fermi energy; thus, the electronic structure is not HM, but the highly spin-polarized values are estimated as P_{DOS} = 98.2 and 89.3%, respectively. On the other hand, negative spin polarization, P_{DOS} = −62.3%, is obtained in Co_2FeSi, where the minority DOS is much greater compared to the majority state at Fermi energy. Note that, as the Y atom is changed from a large atomic number (Z_{Fe} = 26) to small (Z_{V} = 23), the Fermi energy position seems to move away from the conduction state of minority spin, but this is not the case for Y = Ti. This exception is attributable to the fact that the Ti spins in Co_2TiSi couple with those of Co with anti-parallel direction and the ferrimagnetic structure is obtained in our calculations,

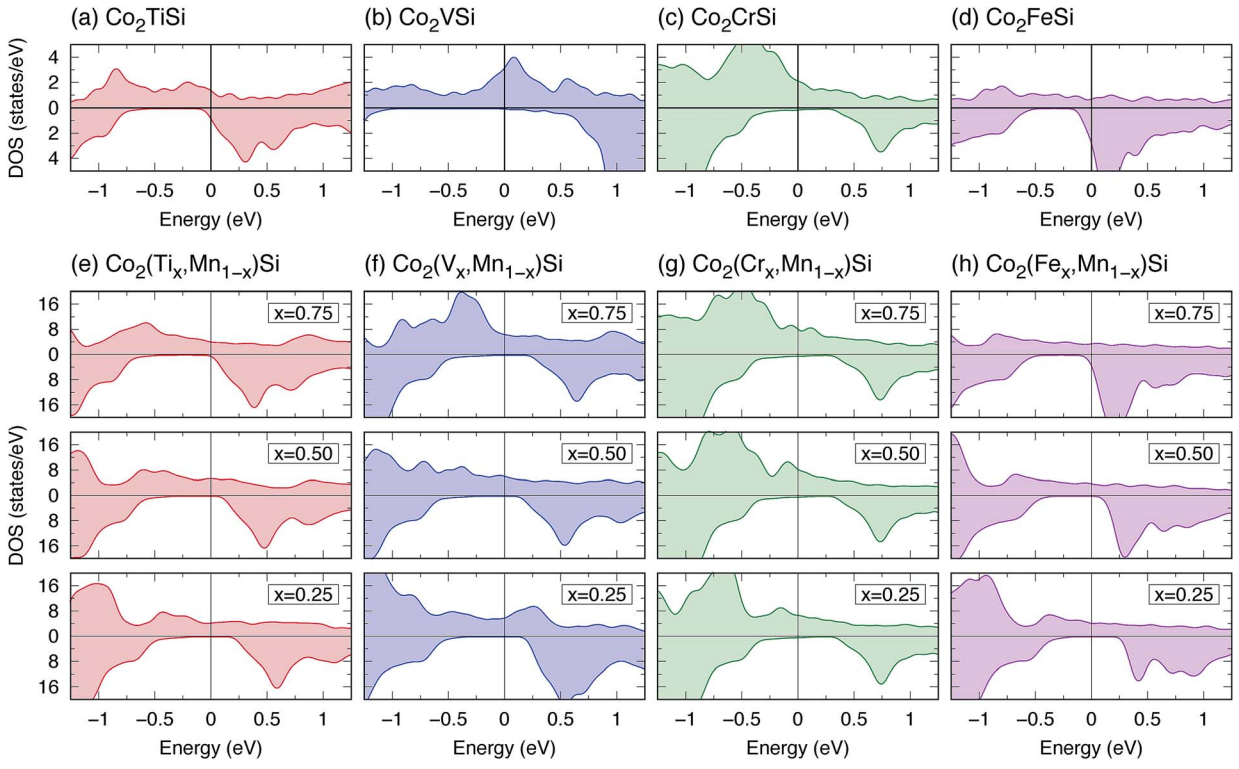

Fig. 9 (a–d) Total DOS for ternary Co_2YSi (Y = Ti, V, Cr, or Fe), and (e–h) total DOS dependence on composition x for quaternary $Co_2(Y_x,Mn_{1-x})Si$ (x = 0.25, 0.5, or 0.75) calculated by the LR-based DFT+U method. In each panel, the upper (bottom) region shows the DOS for up- (down-) spin states, and the Fermi energy is set to zero. Note that the vertical axis range of DOS in (a–d) is different from that in (e–h) as the number of atoms per primitive cell of the ternary system is a quarter of the quaternary one (see Fig. 1).

Table 4 Nominal number of valence electrons N_{val} and calculated spin magnetic moments of total and atom-resolved contributions (in units of μ_B) for Co_2YSi (Y = Ti, V, Cr, or Fe) and $Co_2(Y_x,Mn_{1-x})Si$ (x = 0.25, 0.50, or 0.75). Results are obtained from the LR-based DFT+U method

		Spin magnetic moment			
	N_{val}	Total	Co	Y	Mn
Co_2TiSi	26	1.89	0.97	−0.02	
$Co_2(Ti_{0.75}Mn_{0.25})Si$	26.75	2.76	0.94	−0.09	3.85
$Co_2(Ti_{0.50}Mn_{0.50})Si$	27.5	3.54	0.90	−0.21	3.75
$Co_2(Ti_{0.25}Mn_{0.75})Si$	28.25	4.28	0.83	−0.37	3.69
Co_2VSi	27	3.00	1.26	0.59	
$Co_2(V_{0.75}Mn_{0.25})Si$	27.5	3.51	0.84	1.19	3.75
$Co_2(V_{0.50}Mn_{0.50})Si$	28	4.03	0.38	1.06	3.70
$Co_2(V_{0.25}Mn_{0.75})Si$	28.5	4.56	1.10	0.15	3.13
Co_2CrSi	28	4.03	0.52	2.90	
$Co_2(Cr_{0.75}Mn_{0.25})Si$	28.25	4.28	0.58	2.90	3.63
$Co_2(Cr_{0.50}Mn_{0.50})Si$	28.5	4.52	0.62	2.88	3.61
$Co_2(Cr_{0.25}Mn_{0.75})Si$	28.75	4.77	0.67	2.94	3.63
$Co_2(Fe_{0.25}Mn_{0.75})Si$	29.25	5.27	0.94	2.91	3.65
$Co_2(Fe_{0.50}Mn_{0.50})Si$	29.5	5.55	1.15	2.94	3.69
$Co_2(Fe_{0.75}Mn_{0.25})Si$	29.75	5.58	1.25	2.95	3.75
Co_2FeSi	30	5.42	1.29	2.92	

while the other systems favor the ferromagnetic structure (see Table 4). Total spin magnetic moments are calculated as 1.89, 3.00, 4.03, and 5.42 μ_B for Co_2TiSi, Co_2VSi, Co_2CrSi, and Co_2FeSi, respectively.

The structural properties are also investigated as summarized in Table 5. The estimated lattice constants are in good agreement with the experiments[16,18,102,104] and their error values from the experiments are less than 1% for Co_2TiSi, Co_2VSi, and Co_2FeSi. In Co_2CrSi, the lattice constant of 5.694 Å is close to the previous calculation.[105] The bulk moduli in all models estimated from the LR-based DFT+U method are slightly smaller than those in the previous calculations. This trend is similar to the Co_2MnSi case, and might come from the fact that the previous studies were conducted by standard LSDA[105–109] and GGA.[92] The experimentally measured B_0 is available only for Y = Fe (B_0 = 240 GPa).[104] From our calculations, the B_0 and B_0' in Co_2FeSi are found to be 183.263 GPa and 4.679, respectively. The LSDA calculation[92] shows a reasonably consistent value of B_0 = 241.9 GPa with the experiment, although the GGA calculation[105,107,109] underestimates B_0 (B_0 = 203.5–207.1 GPa). Zhu *et al.*[109] also performed GGA+U calculations, where the empirical parameters of U = 3.5 and J = 0.9 eV for Co and those of U = 3.4 and J = 0.9 eV for Fe were employed, and obtained B_0 = 209.3 GPa and B_0' = 4.67 (the GGA+U results are not shown in Table 5). Therefore, the LSDA calculations might be suitable for the bulk modulus compared to the GGA+U approaches, while it seems to underestimate the lattice constant from the experiments, for example, a_0 = 5.52 Å in Co_2FeSi.[92] However, the LR-based DFT+U method provides reasonable results at least for a_0 values.

We finally investigate the quaternary Heusler compounds of chemical formula $Co_2(Y_x,Mn_{1-x})Si$ (Y = Ti, V, Cr, or Fe) with a composition x (x = 0.25, 0.50, or 0.75). To model these systems in $L2_1$ structure, as illustrated in Fig. 1(b)–(d), cubic primitive cells consisting of 16 atoms are considered. The lattice constant is given by Vegard's law[110,111] using the obtained equilibrium lattice constants for Co_2YSi (a^{CYS}) and Co_2MnSi (a^{CMS}) as $a(x) = xa^{CYS} + (1-x)a^{CMS}$. The correlation parameters of the Mn and Y atoms for quaternary systems at all compositions are assumed to be the values of $U_{eff}^{LR(Mn)}$ and $U_{eff}^{LR(Y)}$, which are determined by the LR theory for ternary Co_2MnSi and Co_2YSi. For the quaternary compounds, in which the atomic position of the different elements is not symmetric as in the ternary system, the structures are geometrically relaxed under the equilibrium lattice constants by force calculations using the Broyden–Fletcher–Goldfarb–Shanno (BFGS) algorithm[112–115] until the forces acting on each atom are minimized below the criterion of 10^{-3} Ry per bohr.

The calculated m_{spin} values for the quaternary alloys are also available in Table 4. In the case of only Y = Ti, the Ti spins are ferrimagnetically coupled with Co and Mn similar to that in the ternary model. The Mn m_{spin} is a large value over 3 μ_B in all systems. Fig. 10 plots the total m_{spin} for ternary and quaternary Co-based full Heusler compounds under study as a function of N_{val} in the system. The Slater–Pauling relation is satisfied in the range of less than 29.5 in N_{val} while being slightly underestimated for the range over N_{val} = 29.5, which corresponds to $Co_2(Fe_{0.75},Mn_{0.25})Si$, and Co_2FeSi.

The results for DOS for quaternary alloys are shown in Fig. 9(e)–(h). A perfectly HM electronic structure (P_{DOS} is equal to

Table 5 Structural parameters of lattice constant a_0, bulk modulus B_0, and its pressure derivative B_0' for Co_2YSi comparing the present study, previous calculations, and experiments. The results of the present study are obtained from the LR-based DFT+U method with parameters of $U_{eff}^{LR(Y)}$ = 2.942, 3.979, 3.169, and 3.922 eV for Y = Ti, V, Cr, and Fe, respectively. Previous calculation results are from GGA, except for the bottom row for Co_2FeSi that are from LSDA

	Present work			Theory			Experiment	
	a_0 (A)	B_0 (GPa)	B_0'	a_0 (A)	B_0 (GPa)	B_0'	a_{Expt} (A)	B_0 (GPa)
Co_2TiSi	5.774	189.494	4.191	5.764[a]	204–244.8304[a,b,c,e]	4.5151[e]	5.743[g]	
Co_2VSi	5.667	192.408	7.485	5.7609[b], 5.679[c]	216[b], 221.5[c]		5.647[h]	
Co_2CrSi	5.694	174.169	5.106	5.6295[b], 5.638[c]	227[b], 225.3[c]			
Co_2FeSi	5.685	183.263	4.679	5.6431[b] 5.52[d]	203.5–207.1[b,c,f] 241.9[d]	4.62[f]	5.644[i], 5.650[j]	240[j]

[a] Ref. 106. [b] Ref. 105. [c] Ref. 107. [d] Ref. 92. [e] Ref. 108. [f] Ref. 109. [g] Ref. 16. [h] Ref. 18. [i] Ref. 102. [j] Ref. 104.

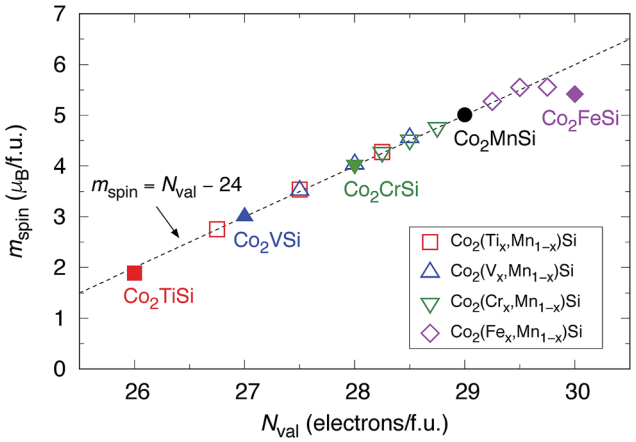

Fig. 10 Total m_{spin} as a function of N_{val} for ternary Co_2YSi (Y = Ti, V, Cr, or Fe) and quaternary $Co_2(Y_x,Mn_{1-x})Si$ (x = 0.25, 0.5, or 0.75). Closed square (red), triangle (blue), down-pointing triangle (green), and diamond (pink) indicate ternary systems, respectively. Opened symbols are for quaternary systems. The results of Co_2MnSi are also plotted using a closed circle (black). The Slater–Pauling relation, $m_{spin} = N_{val} - 24$, is shown by a dotted line.

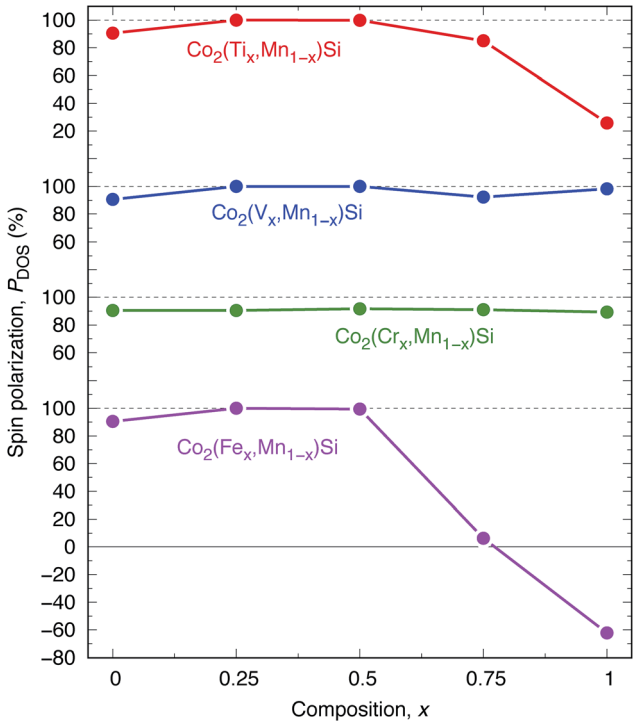

Fig. 11 Spin polarization P_{DOS} dependence on composition x in $Co_2(Y_x,Mn_{1-x})Si$. Red, blue, green, and pink plots are Y of Ti, V, Cr, and Fe, respectively.

100%) is found in $Co_2(Ti_{0.25},Mn_{0.75})Si$, $Co_2(V_{0.25},Mn_{0.75})Si$, $Co_2(V_{0.50},Mn_{0.50})Si$, and $Co_2(Fe_{0.25},Mn_{0.75})Si$. Among them, $Co_2(V_{0.75},Mn_{0.25})Si$ has the largest minority band gap $E_{gap}^{\downarrow} = 0.5$ eV, and thus, this material can be a good candidate for a wide-gap HM ferromagnet. $Co_2(Ti_{0.25},Mn_{0.75})Si$ and $Co_2(Fe_{0.25},Mn_{0.75})Si$ are also HM candidates because of the advantage in Fermi energy position, as it locates at almost the center of the valence and conduction states in minority states. These HM characters lead to the robustness of spin polarization due to the broadening of valence and conduction states at finite temperature. Nearly HM (P_{DOS} is almost 100%) is found in $Co_2(Ti_{0.50},Mn_{0.50})Si$ (P_{DOS} = 99.9%) and $Co_2(Fe_{0.50},Mn_{0.50})Si$ (99.4%). Fig. 11 presents the composition dependence of P_{DOS}. Although the Y = Cr system does not show the HM property at each composition, an interesting trend we observed is that a high P_{DOS} is independent of the composition, and Y = V is also the same, whereas a large reduction of P_{DOS} occurs with an increase in x in the other systems, especially for $Co(Fe_x,Mn_{1-x})Si$.

Finally, we state the results of systems including Fe by comparing with previous studies. Whether the electronic structure of the Co_2FeSi compound shows HM is still under debate and has been for the past few decades, considering theories both with and without correlation effects.[17,116] Our LR-based DFT+U calculations indicate that it is not a HM ferromagnet. However, we emphasize that tuning the composition in quaternary $Co_2(Fe,Mn)Si$ demonstrates that the electronic structure can be HM. This conclusion is supported by a consistency in anisotropic magnetoresistance (AMR) measurement.[117] According to an extended model for AMR formulated by Kokado *et al.*, the negative sign of the AMR effect arising from the empty DOS, either spin-up or -down states, at the Fermi level is a signature of HM.[118–120] Based on this model analysis, positive AMR behavior is found in Co_2FeSi[117], which indicates a ferromagnetic without the minority band gap, but the negative sign is confirmed in $Co_2(Fe,Mn)Si$,[121] leading to HM. Note that the composition range of Fe and Mn for $Co_2(Fe,Mn)Si$, showing HM, is different between our study and the AMR experiment, which may be because the present quaternary models [Fig. 1(b)–(d)] are assumed to be a periodic structure not including the disordered properties of Fe and Mn, and/or the ordering parameter of the $L2_1$ structure in the experiment[117] is rather low at all compositions. Nonetheless, we suggest that the quaternary $Co_2(Fe_{0.25},Mn_{0.75})Si$ is one of the most promising candidates as an HM Heusler ferromagnet because of the sizable $E_{gap}^{\downarrow}$(=0.4 eV) and the Fermi energy position being at almost the center of the gap. We believe our present results encourage experiments to improve the degree of crystallinity of bulk Heusler alloys and/or to fabricate a clean interface without any atomic inter-diffusion in MTJ and CPP-GMR devices for the enhancement of MR performances in the future.

5 Summary

In summary, we revisited the fundamental electronic structure and effects of the correlation parameters for 3d electrons in a Co-based full Heusler Co_2YSi alloy *via* the LR-based DFT+U method, where the correlation correction U_{eff} parameters were determined from the LR approach and the +U formalism was incorporated as the FLL form. Focusing on Co_2MnSi (Y = Mn), we considered the origin of the minority HM gap from the projected band structures calculated by the standard GGA, and found that the t_{2g} hybridization between Co and Mn is important for the gap. The energy diagram of atomic-orbital

hybridizations revealed that the HM gap originates from the Co e_u^* of the conduction state and the Co–Mn hybridizing t_{2g} orbitals of the valence state at the Fermi energy. Thus, the gap is tunable by selecting a Y element and/or mixing different elements into the Y site through t_{2g} atomic orbital coupling. The LR calculations tend to obtain a reasonable value as a correlation parameter for the Y site (Y = Mn in Co_2MnSi) but an unexpectedly large value for the Co site, which misleads to an unphysical ground state. The failure in determining U_{eff}^{LR} for the Co site arises from the fact that the d electrons of the Co site behave in a rather itinerant fashion in the alloy. This means that the mean-field approximations such as LSDA and GGA are enough to describe the ground-state properties with high accuracy; thus, we propose the LR-based DFT+*U* method, where the determined U_{eff}^{LR} parameters are incorporated into only strongly-correlated Y sites, as a suitable methodology on a practical level for $L2_1$ Co-based full Heusler alloys. For Co_2-MnSi, our results are consistent with the experimental observations and superior to the standard GGA calculation, particularly in terms of electronic and magnetic properties. It is also indicated that Co_2MnSi is not HM but a highly spin-polarized ferromagnet. Further investigations were carried out for the other ternary and quaternary Co_2(Y,Mn)Si to explore the potential for HM ferromagnets. The results showed that the Co_2(Ti,Mn)Si, Co_2(V,Mn)Si, and Co_2(Fe,Mn)Si compounds are expected to be HM materials when the composition of the Y element is appropriately selected. Co_2(-Cr,Mn)Si does not show the HM property at every composition, but a notable tendency is that the high spin polarization is independent of the composition. However, for using in spintronics applications, $Co_2(Fe_{0.25},Mn_{0.75})Si$, in which the HM nature is consistent with the experimental AMR study, is one of the most promising candidates because of the sizable HM gap in the minority state and as the Fermi energy position is at almost the center of the gap.

Conflicts of interest

There are no conflicts to declare.

Acknowledgements

The authors are grateful to K. Masuda, H. Sukegawa, and S. Mitani for critical comments and suggestions. K. N. also thanks K. Nakamura, T. Oguchi, and M. Weinert for fruitful discussions. This work was supported in part by Grants-in-Aid for Scientific Research (S) (Grant Numbers JP16H06332 and JP17H06152) from the Japan Society for the Promotion of Science, the ImPACT Program of Council for Science, Technology and Innovation, 'Materials Research by Information Integration Initiative (Mi^2i)' Project of the Support Program for Starting Up Innovation Hub from Japan Science and Technology Agency (JST), and Center for Spintronics Research Network (CSRN), Osaka University. The computations in this study were performed on a Numerical Materials Simulator at NIMS.

References

1 M. Jullière, *Phys. Lett. A*, 1975, **54**, 225.
2 I. Galanakis, *Phys. Rev. B: Condens. Matter Mater. Phys.*, 2002, **66**, 012406.
3 W.-H. Xie, Y.-Q. Xu, B.-G. Lie and D. G. Pettifor, *Phys. Rev. Lett.*, 2003, **91**, 037204.
4 B.-G. Lie, *Phys. Rev. B: Condens. Matter Mater. Phys.*, 2003, **67**, 172411.
5 W. E. Pickett and D. J. Singh, *Phys. Rev. B: Condens. Matter Mater. Phys.*, 1996, **53**, 1146.
6 D. J. Singh and W. E. Pickett, *Phys. Rev. B: Condens. Matter Mater. Phys.*, 1998, **57**, 88.
7 K. Schwarz, *J. Phys. F: Met. Phys.*, 1986, **16**, L211.
8 H. van Leuken and R. A. de Groot, *Phys. Rev. B: Condens. Matter Mater. Phys.*, 1998, **51**, 7176.
9 S. P. Lewis, P. B. Allen and T. Sasaki, *Phys. Rev. B: Condens. Matter Mater. Phys.*, 1997, **55**, 10253.
10 M. A. Korotin, V. I. Anisimov, D. I. Khomskii and G. A. Sawatzky, *Phys. Rev. Lett.*, 1998, **80**, 4305.
11 R. A. de Groot and K. H. J. Buschow, *J. Magn. Magn. Mater.*, 1986, **54–57**, 1377.
12 M. Pénicaud, B. Siberchicot, C. B. Sommers and J. Kübler, *J. Magn. Magn. Mater.*, 1992, **103**, 212.
13 B. Chakraborty and L. M. Ramaniah, *J. Magn. Magn. Mater.*, 2015, **1385**, 207.
14 B. Chakraborty and L. M. Ramaniah, *J. Phys.: Condens. Matter*, 2016, **28**, 336001.
15 B. Chakraborty, P. K. Nandi, Y. Kawazoe and L. M. Ramaniah, *Phys. Rev. B*, 2018, **97**, 184411.
16 K. H. J. Bushow, P. G. v. Engen and R. Jogebreur, *J. Magn. Magn. Mater.*, 1983, **38**, 1.
17 S. Wurmehl, G. H. Fecher, H. C. Kandpal, V. Ksenofontov, C. Felser, H.-J. Lin and J. Morais, *Phys. Rev. B: Condens. Matter Mater. Phys.*, 2005, **72**, 184434.
18 S. Wurmehl, G. H. Fecher, H. C. Kandpal, V. Ksenofontov, C. Felser and H.-J. Lin, *Appl. Phys. Lett.*, 2006, **88**, 032503.
19 Y. Sakuraba, J. Nakata, M. Oogane, H. Kubota, Y. Ando, A. Sakuma and Y. Miyazaki, *Jpn. J. Appl. Phys.*, 2005, **44**, L1100.
20 Y. Sakuraba, M. Hattori, M. Oogane, Y. Ando, H. Kato, A. Sakuma and T. Miyazaki, *Appl. Phys. Lett.*, 2006, **88**, 192508.
21 B. Hu, K. Moges, Y. Honda, H. X. Liu, T. Uemura, M. Yamamoto, J. I. Inoue and M. Shirai, *Phys. Rev. B*, 2016, **94**, 094428.
22 W. H. Butler, X.-G. Zhang, T. C. Schulthess and J. M. MacLaren, *Phys. Rev. B: Condens. Matter Mater. Phys.*, 2001, **63**, 054416.
23 R. J. Soulen, J. M. Byers, M. S. Osofsky, B. Nadgorny, T. Ambrose, S. F. Cheng, P. R. Broussard, C. T. Tanaka, J. Nowak, K. S. Moodera, A. Barry and J. M. D. Coey, *Science*, 1998, **282**, 85.
24 M. S. Bahramy, P. Murugan, G. P. Das and Y. Kawazoe, *Phys. Rev. B: Condens. Matter Mater. Phys.*, 2007, **75**, 054404.
25 A. Rajanikanth, Y. K. Takahashi and K. Hono, *J. Appl. Phys.*, 2009, **105**, 063916.

26 Z. Gercsi, A. Rajanikanth, Y. K. Takahashi and K. Hono, *Appl. Phys. Lett.*, 2007, **89**, 082512.
27 S. V. Karthik, A. Rakanikanth and T. M. Nakatani, *J. Appl. Phys.*, 2007, **102**, 043903.
28 L. Makinistian, M. M. Faiz, R. P. Panguluri, B. Balke, S. Wurmehl, C. Felser, E. A. Albanesi, A. G. Petukhov and B. Nadgorny, *Phys. Rev. B: Condens. Matter Mater. Phys.*, 2013, **87**, 220402.
29 L. Bainsla, A. I. Mallick, M. M. Raja, A. K. Nigam, B. S. D. Ch. S. Varaprasad, Y. K. Takahashi, A. Alam, K. G. Suresh and K. Hono, *Phys. Rev. B: Condens. Matter Mater. Phys.*, 2015, **91**, 104408.
30 Y. Sakuraba, M. Ueda, S. Bosu, K. Saito and K. Takanashi, *J. Magn. Soc. Jpn.*, 2014, **38**, 45.
31 S. Tsunegi, Y. Sakuraba, M. Oogane, K. Takanashi and Y. Ando, *Appl. Phys. Lett.*, 2008, **93**, 112506.
32 Y. Sakuraba, M. Ueda, Y. Miura, K. Sato, S. Bosu, K. Saito, M. Shirai, T. J. Konno and K. Takanashi, *Appl. Phys. Lett.*, 2012, **101**, 252408.
33 K. Moges, Y. Honda, H. X. Liu, T. Uemura, M. Yamamoto, Y. Miura and M. Shirai, *Phys. Rev. B*, 2016, **93**, 134403.
34 H. Liu, T. Kawami, K. Moges, T. Uemura, M. Yamamoto, F. Shi and P. M. Voyles, *J. Phys. D: Appl. Phys.*, 2015, **48**, 164001.
35 P. Hohenberg and W. Kohn, *Phys. Rev.*, 1964, **136**, B864.
36 W. Kohn and L. J. Sham, *Phys. Rev.*, 1965, **140**, A1133.
37 W. Kohn, *Rev. Mod. Phys.*, 1999, **71**, 1253.
38 I. Galanakis, P. H. Dederichs and N. Papanikolaou, *Phys. Rev. B: Condens. Matter Mater. Phys.*, 2002, **66**, 174429.
39 R. A. de Groot, F. M. Mueller, P. G. van Engen and K. H. J. Buschow, *Phys. Rev. Lett.*, 1983, **50**, 2024.
40 K. Schwarz, *J. Phys. F: Met. Phys.*, 1986, **16**, L211.
41 S. Ishida, S. Fujii, S. Kashiwagi and S. Asano, *J. Phys. Soc. Jpn.*, 1995, **64**, 2152.
42 S. Picozzi, A. Continenza and A. J. Freeman, *Phys. Rev. B: Condens. Matter Mater. Phys.*, 2002, **66**, 094421.
43 M. Shirai, *J. Appl. Phys.*, 2003, **93**, 6844.
44 E. Şaşioğlu, L. M. Sandratskii, P. Bruno and I. Galanakis, *Phys. Rev. B: Condens. Matter Mater. Phys.*, 2005, **72**, 184415.
45 V. I. Anisimov, A. I. Poteryaev, M. A. Korotin, A. O. Anokhin and G. Kotliar, *J. Phys.: Condens. Matter*, 1997, **9**, 7359.
46 A. I. Lichtenstein and M. I. Katsnelson, *Phys. Rev. B: Condens. Matter Mater. Phys.*, 1998, **57**, 6884.
47 J. P. Perdew, M. Ernzerhof and K. Burke, *J. Chem. Phys.*, 1996, **105**, 9982.
48 S. Kobayashi, Y. Nohara, S. Yamamoto and T. Fujiwara, *Phys. Rev. B: Condens. Matter Mater. Phys.*, 2008, **78**, 155112.
49 H. Jiang, R. I. Gomez-Abal, P. Rinke and M. Scheffler, *Phys. Rev. Lett.*, 2009, **102**, 126403.
50 V. I. Anisimov, J. Zaanen and O. K. Andersen, *Phys. Rev. B: Condens. Matter Mater. Phys.*, 1991, **44**, 943.
51 V. I. Anisimov, F. Aryasetiawan and A. I. Liechtenstein, *J. Phys.: Condens. Matter*, 1997, **9**, 767.
52 M. I. Katsnelson, V. Yu. Irkhin, L. Chioncel, A. I. Lichtenstein and R. A. de Groot, *Rev. Mod. Phys.*, 2008, **80**, 315.
53 S. Chadov, G. H. Fecher, C. Felser, J. Minar, J. Braun and H. Ebert, *J. Phys. D: Appl. Phys.*, 2009, **42**, 084002.
54 A. Nourmohammadi and M. R. Abolhasani, *Solid State Commun.*, 2010, **150**, 1501.
55 M. Meinert, C. Friedrich, G. Reiss and S. Blügel, *Phys. Rev. B: Condens. Matter Mater. Phys.*, 2012, **86**, 245115.
56 J. Hubbard, *Proc. R. Soc. London, Ser. A*, 1965, **285**, 542.
57 J. Hubbard, *Proc. R. Soc. London, Ser. A*, 1967, **296**, 82.
58 K. Nawa, T. Akiyama, T. Ito, K. Nakamura, T. Oguchi and M. Weinert, *Phys. Rev. B*, 2018, **97**, 035117.
59 M. Cococcioni and S. de Gironcoli, *Phys. Rev. B: Condens. Matter Mater. Phys.*, 2005, **71**, 035105.
60 F. Zhou, M. Cococcioni, C. A. Marianetti, D. Morgan and G. Ceder, *Phys. Rev. B: Condens. Matter Mater. Phys.*, 2004, **70**, 235121.
61 B. Himmetoglu, R. M. Wentzcovitch and M. Cococcioni, *Phys. Rev. B: Condens. Matter Mater. Phys.*, 2011, **84**, 115108.
62 K. Tao, J. Zhou, Q. Sun, Q. Wang, V. S. Stepanyuk and P. Jena, *Phys. Rev. B: Condens. Matter Mater. Phys.*, 2014, **89**, 085103.
63 A. G. Marinopoulos, P. Santos and J. Coutinho, *Phys. Rev. B: Condens. Matter Mater. Phys.*, 2015, **92**, 075124.
64 X. Huang, S. K. Ramadugu and S. E. Mason, *J. Phys. Chem. C*, 2016, **120**, 4919.
65 K. Nawa, Y. Kitaoka, K. Nakamura, H. Imamura, T. Akiyama, T. Ito and M. Weinert, *Phys. Rev. B*, 2016, **94**, 035136.
66 B. Himmetoglu, V. M. Katukuri and M. Cococcioni, *J. Phys.: Condens. Matter*, 2012, **24**, 185501.
67 P. Giannozzi, *et al.*, *J. Phys.: Condens. Matter*, 2009, **21**, 395502; S. Baroni, A. Dal Corso, S. de Gironcoli and P. Giannozzi, http://www.pwscf.org.
68 A. M. Rappe, K. M. Rabe, E. Kaxiras and J. D. Joannopoulos, *Phys. Rev. B: Condens. Matter Mater. Phys.*, 1990, **41**, 1227.
69 Because even the theoretically derived U_{eff} value depends on the computational details, as discussed in ref. 58, we explicitly specify which pseudopotential is employed in the present study: Si.pbe-n-rrkjus_psl.0.1.UPF; Ti.pbe-spn-rrkjus_psl.0.3.1.UPF; V.pbe-spn-rrkjus_psl.0.2.3.UPF; Cr.pbe-spn-rrkjus_psl.0.2.3.UPF; Mn.pbe-spn-rrkjus_psl.0.3.1.UPF; Fe.pbe-spn-rrkjus_psl.0.2.1.UPF; and Co.pbe-n-rrkjus_psl.0.2.3.UPF. The used pseudopotential scheme given in ref. 68 is known to beappropriate for 3d transition metal and non-magnetic sp atoms.
70 A. Baldereschi, *Phys. Rev. B: Solid State*, 1973, **7**, 5212; D. J. Chadi and M. L. Cohen, *Phys. Rev. B: Solid State*, 1973, **8**, 5747; H. J. Monkhorst and J. D. Pack, *Phys. Rev. B: Solid State*, 1976, **13**, 5188; J. D. Pack and H. J. Monkhorst, *Phys. Rev. B: Solid State*, 1977, **16**, 1748.
71 M. Methfessel and A. T. Paxton, *Phys. Rev. B: Condens. Matter Mater. Phys.*, 1989, **40**, 3616.
72 I. Galanakis, *Phys. Rev. B: Condens. Matter Mater. Phys.*, 2005, **71**, 012413.
73 Ph. Mavropoulos, K. Sato, R. Zeller, P. H. Dederichs, V. Popescu and H. Ebert, *Phys. Rev. B: Condens. Matter Mater. Phys.*, 2005, **71**, 012413.

74 Ph. Mavropoulos, I. Galanakis, V. Popescu and P. H. Dederichs, *J. Phys.: Condens. Matter*, 2004, **16**, S5759.
75 J. P. Perdew, K. Burke and M. Ernzerhof, *Phys. Rev. Lett.*, 1996, **77**, 3865.
76 A. I. Liechtenstein, V. I. Anisimov and J. Zaanen, *Phys. Rev. B: Condens. Matter Mater. Phys.*, 1995, **52**, R5467.
77 V. I. Anisimov, I. V. Solovyev, M. A. Korotin, M. T. Czyźyk and G. A. Sawatzky, *Phys. Rev. B: Condens. Matter Mater. Phys.*, 1993, **48**, 16929.
78 M. T. Czyźyk and G. A. Sawatzky, *Phys. Rev. B: Condens. Matter Mater. Phys.*, 1994, **49**, 14211.
79 I. V. Solovyev, P. H. Dederichs and V. I. Anisimov, *Phys. Rev. B: Condens. Matter Mater. Phys.*, 1994, **50**, 16861.
80 C. Tsirogiannis and I. Galanakis, *J. Magn. Magn. Mater.*, 2015, **393**, 297.
81 S. L. Dudarev, G. A. Botton, S. Y. Savrasov, C. J. Humphreys and A. P. Sutton, *Phys. Rev. B: Condens. Matter Mater. Phys.*, 1998, **57**, 1505.
82 V. I. Anisimov, F. Aryasetiawan and A. I. Lichtenstein, *J. Phys.: Condens. Matter*, 1997, **9**, 767.
83 J. P. Perdew, R. G. Parr, M. Levy and J. L. Balduz, *Phys. Rev. Lett.*, 1982, **49**, 1691.
84 J. P. Perdew and M. Levy, *Phys. Rev. Lett.*, 1983, **51**, 1884.
85 L. J. Sham and M. Schlüter, *Phys. Rev. Lett.*, 1983, **51**, 1888.
86 A. Akriche, H. Bouafia, S. Hiadsi, B. Abidri, B. Sahli, M. Elchikh, M. A. Timaoui and B. Djebour, *J. Magn. Magn. Mater.*, 2017, **422**, 13.
87 E. Şaşioğlu, I. Galanakis, C. Friedrich and S. Blügel, *Phys. Rev. B: Condens. Matter Mater. Phys.*, 2013, **88**, 134402.
88 In order to consider the effect of size of applied potential shift, various values of μ_{Co} were tested to compute the $U_{eff}^{LR(Co)}$, for example, $\mu_{Co} = \pm 0.06$, ± 0.1, ± 0.5, ± 1.0, and ± 2.0 eV. The obtained parameters are almost same with differences less than 0.05 eV with an exception of the $\mu_{Co} = \pm 2.0$ eV case, where the stationary self-consistent solution was not obtained because of the too large potential shift.
89 B. Huang, *Phys. Chem. Chem. Phys.*, 2017, **19**, 8008.
90 A. G. Petukhov, I. I. Mazin, L. Chioncel and A. I. Lichtenstein, *Phys. Rev. B: Condens. Matter Mater. Phys.*, 2003, **67**, 153106.
91 F. D. Murnaghan, *Proc. Natl. Acad. Sci. U. S. A.*, 1944, **30**, 244.
92 J. N. Gonçalves, J. S. Amaral and V. S. Amaral, *IEEE Trans. Magn.*, 2014, **50**, 1301104.
93 A. Candan, G. Uğur, Z. Charifi, H. Baaziz and M. R. Ellialtioğlu, *J. Alloys Compd.*, 2013, **560**, 25.
94 G. Gökoğlu and O. Gülseren, *Eur. Phys. J. B*, 2010, **76**, 321.
95 S. Amuri, R. Mebsout, S. Méçabih, B. Abbar and B. Bouhafs, *Intermetallics*, 2014, **44**, 26.
96 P. J. Webster, *J. Phys. Chem. Solids*, 1971, **32**, 1221.
97 H. Ido, *J. Magn. Magn. Mater.*, 1986, **54**, 937.
98 B. Balke, G. H. Fecher, H. C. Kandpal, C. Felser, K. Kobayashi, E. Ikenaga, J.-J. Kim and S. Ueda, *Phys. Rev. B: Condens. Matter Mater. Phys.*, 2006, **74**, 104405.
99 P. Klaer, M. Kallmayer, C. G. F. Blum, T. Graf, J. Barth, B. Balke, G. H. Fecher, C. Felser and H. J. Elmers, *Phys. Rev. B: Condens. Matter Mater. Phys.*, 2009, **80**, 144405.
100 K. Miyamoto, A. Kimura, Y. Miura, M. Shirai, M. Ye, Y. Cui, K. Shimada, H. Namatame, M. Taniguchi, Y. Takeda, Y. Saitoh, E. Ikenaga, S. Ueda, K. Kobayashi and T. Kanomata, *Phys. Rev. B: Condens. Matter Mater. Phys.*, 2009, **79**, 100405.
101 T. Kanomata, *et al.*, *Heusler alloy as a functional material*, Uchida Rokakuho, Tokyo, 2011.
102 E. I. Gladyshevskii, *Powder Metall. Met. Ceram.*, 1983, **1**, 262.
103 The LR calculations were also done for the $U_{eff}^{LR(Co)}$ in Co_2YSi. Similar to Co_2MnSi, large values of 6.536, 6.563, 6.674, and 5.782 eV are obtained for Co of Co_2YSi, where Y is Ti, V, Cr, and Fe, respectively. Based on the discussion in Section 3, the U_{eff}^{LR} values for Co are not used for the calculations in the present work.
104 A. B. Garg and V. Vijayakumar, *J. Appl. Phys.*, 2011, **100**, 083523.
105 X.-Q. Chen, R. Podloucky and P. Rogl, *J. Appl. Phys.*, 2006, **100**, 113901.
106 S. M. Mareii, H. Arabi and R. Sarhaddi, *Physica B*, 2012, **407**, 3339.
107 S. C. Wu, G. H. Fecher, S. S. Naghari and C. Felser, *J. Appl. Phys.*, 2019, **125**, 082523.
108 I. Asfour, D. Rached, A. Girard soraya and S. Didier, *Universal Journal of Mechanical Engineering*, 2019, **7**, 16.
109 X. Zhu, Y. Wang, L. Wang, Y. Dai and C. Luo, *J. Phys. Chem. Solids*, 2014, **75**, 391.
110 L. Vegard, *Z. Phys.*, 1920, **5**, 17.
111 A. R. Denton and N. W. Ashcroft, *Phys. Rev. A: At., Mol., Opt. Phys.*, 1991, **43**, 3161.
112 C. G. Broyden, *SIAM J. Appl. Math.*, 1970, **6**, 76.
113 R. Fletcher, *Comput. J.*, 1970, **13**, 317.
114 D. Goldfarb, *Math. Comput. Model.*, 1970, **24**, 24.
115 D. F. Shanno, *Math. Comput. Model.*, 1970, **24**, 647.
116 H. C. Kandpal, G. H. Fecher, C. Felser and G. Schönhense, *Phys. Rev. B: Condens. Matter Mater. Phys.*, 2006, **73**, 094422.
117 Y. Sakuraba, S. Kokado, Y. Hirayama, T. Furubayashi, H. Sukegawa, S. Li, Y. K. Takahashi and K. Hono, *Appl. Phys. Lett.*, 2014, **104**, 172407.
118 S. Kokado, M. Tsunoda, K. Harigaya and A. Sakumra, *J. Phys. Soc. Jpn.*, 2012, **81**, 024705.
119 S. Kokado and M. Tsunoda, *Adv. Mater. Res.*, 2013, **750**, 978.
120 S. Kokado and M. Tsunoda, *Phys. Status Solidi C*, 2014, **11**, 1026.
121 F. J. Yang, Y. Sakuraba, S. Kokado, Y. Kota, A. Sakuma and K. Takanashi, *Phys. Rev. B: Condens. Matter Mater. Phys.*, 2012, **86**, 020409.